Measurement of the Polarization of the Cosmic Microwave Background

Thesis by

Byron J. Philhour

In Partial Fulfillment of the Requirements

for the Degree of

Doctor of Philosophy

California Institute of Technology

Pasadena, California

2002

(Submitted January 4, 2002)

Acknowledgments

> "Each discovery, each advance, each increase in the sum of human riches, owes its being to the physical and mental travail of the past and the present. By what right then can any one whatever appropriate the least morsel of this immense whole and say – This is mine, not yours?"
> — P. Kropotkin, *The Conquest of Bread*

Abstract

Measurement of cosmic microwave background (CMB) polarization will provide a powerful check on the model that describes CMB ΔT fluctuations as arising from density fluctuations in the early universe, break degeneracies between cosmological parameters that arise in interpreting ΔT fluctuations, and may ultimately allow detection of the stochastic gravity-wave background predicted by inflationary models. We describe the development and laboratory characterization of a bolometric experiment designed to measure the arcminute-scale polarization of the CMB. The Polatron receiver will be mounted at the Cassegrain focus of the 5.5 m telescope at the Owens Valley Radio Observatory. The receiver will measure both the Q and U Stokes parameters over a 20% pass-band centered near 100 GHz, with the input polarization signal modulated at $\sim$ 1 Hz by a rotating, birefringent, quartz half-wave plate. In six months of observation we plan to observe $\sim$ 400 2.5 arcminute pixels in a ring about the North Celestial Pole to a precision of $\sim$ 5 μK per pixel in each of Q and U, adequate to unambiguously detect CMB polarization at levels predicted by current models.

Contents

List of Figures

List of Tables

Chapter 1   Cosmology and the Cosmic Microwave Background

1.1   Introduction

The Big Bang model of cosmological evolution has provided a compelling solution to the paradox popularized almost two hundred years ago by amateur astronomer Heinrich Olbers: "Warum ist es nachts dunkel?" – Why is night-time dark? The paradox rests on two assumptions. First, it assumes that the universe is infinite in time and space, so that every line of sight should eventually intersect a luminous object. Second, it observes that the night-time sky is, in fact, dark. The discovery by Edwin Hubble in 1929 [32] that space is expanding led to a rethinking of the first assumption: if galaxies are moving apart, they were once much closer together; hence, the universe has a finite age, and the observable universe a finite size. The discovery by Arno Penzias and Robert Wilson in 1964 of cosmic microwave background (CMB) radiation [57] led to a rethinking of the second assumption: the night sky is not dark! Every unobstructed line of sight eventually *does* intersect a luminous object, namely the primordial fireball that is the universe in its early, dense, hot state. Expansion of space merely shifts the emission spectrum of that fireball from visual to microwave wavelengths.

The CMB is a remarkable tool. For example, the physical dimensions of distant galaxy clusters can be measured by interpreting arcminute-scale millimeter-wave intensity decrements at the cluster as up-scattering of CMB photons by a hot intracluster gas [71, 28]. The observed dipole anisotropy in the CMB reveals the peculiar velocity of the Milky Way [70]. Slight temperature anisotropies ($\Delta T/T \sim 10^{-5}$) on large angular scales reveal scale-invariance in the density inhomogeneities of the early universe, a prediction of inflation models [70]. Furthermore, recently obtained
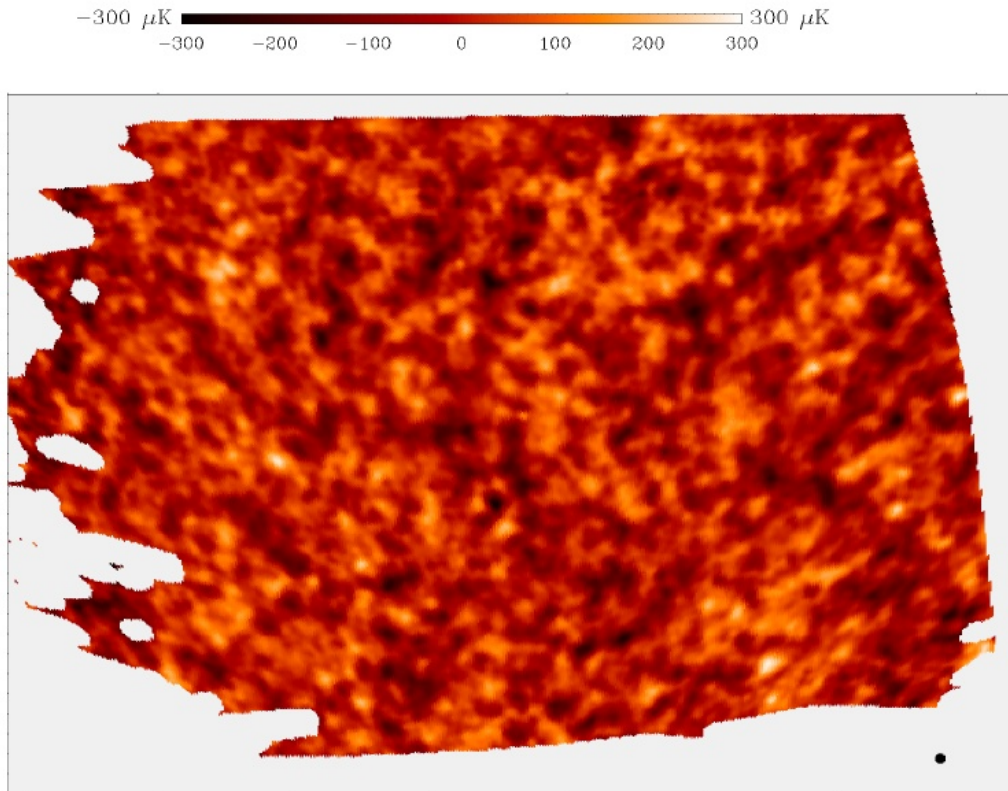
Figure 1.1: Map of CMB temperature fluctuations about the mean CMB temperature, 2.728 K, as measured by the BOOMERANG instrument in its Antarctic balloon flight of 1998. Some spatial filtering has been applied; see papers referenced in text for details. Black dot in lower right-hand corner is the angular size of the Moon ($\sim \frac{1}{2}^{\circ}$). Figure was obtained from the BOOMERANG web site.

high resolution maps of the CMB, such as the BOOMERANG map shown in Figure 1.1, reveal acoustic peaks in the angular power spectrum (Figure 1.5). Data from BOOMERANG, MAXIMA, DASI, and other experiments have recently been used to constrain a variety of cosmological models, as well as provide accurate cosmological parameters for cold dark matter (CDM) evolutionary models [41, 13, 62, 73]. The density inhomogeneities these measurements have unveiled are believed to be the seeds of the gravity-enhanced structures we see in the universe today.

Measurement of CMB polarization is complementary to, and an extension of, measurements of CMB ΔT fluctuations. Temperature anisotropies induced by density

fluctuations in the early universe should themselves generate measurable CMB polarization [33, 30]. Cosmological models that predict the temperature angular power spectra predict corresponding polarization angular power spectra. As discussed in §1.3, measurement of the pattern and amplitude of CMB polarization will enable us to do the following:

- Check the consistency of the paradigm that describes CMB ΔT fluctuations as arising from density fluctuations in the early universe (t $\sim$ 300,000 yr). Unlike temperature fluctuations, polarization of the CMB can only be generated or modified by scattering (see §1.3).

- Break degeneracies between cosmological parameters that arise in interpreting ΔT fluctuations. For example, it is difficult to use ΔT information alone to distinguish between dilution of signal at large angular scales due to reionization and an overall change in the normalization of the primordial power spectrum. However, late reionization should produce a recognizable signal — *more* power at large angular scales — in polarization [38].

- Test for the presence of the stochastic gravity-wave background predicted by inflation models [60, 35, 68, 36]. Should they exist, primordial gravity waves would carry information from an inflationary era never before open to investigation, and encode such information in a curl component to the CMB polarization vector pattern.

CMB polarization has never been detected. The status of this developing field is analogous to that of ΔT measurements ten to fifteen years ago, with even the most sensitive upper limits an order of magnitude above the theoretically expected signal (§1.5). This situation is set to change soon with the ongoing deployment of a new generation of experiments specifically designed to measure CMB polarization (§1.6).

The remainder of Chapter 1 is devoted to the introduction of CMB polarization as a probe of cosmological parameters, and a framework for the description of polarization is provided. A review of the status and direction of the field is included.

Chapter 2 describes one experiment under construction, the Polatron, which is designed to measure CMB polarization. In Chapter 3, the development of the cryogenic system of the Polatron receiver receives a closer look; construction of an adequate cryogenic system has been the focus of enormous effort on the part of the Polatron team. Chapter 4 contains a calculation of the expected sensitivity of the Polatron and describes the observing strategy we will employ to reduce systematic effects. Chapters 5 and 6 are devoted to the laboratory characterization of the instrument. The former describes the optical system and polarization characteristics; the latter briefly describes the cryogenic performance of the system. In Chapter 7, we discuss these results and outline the future of the Polatron experiment. A technical appendix describing the calculation of the polarization efficiency of half-wave plates is also included.

1.2   Polarization Formalism

We begin with a formal description of the polarization of light. A photon travelling in the $\hat{z}$ direction with wavelength λ and frequency ν can be described by an electric field vector

$$
\begin{aligned}
\overrightarrow{E}(x, y, z, t) &= E_x(t) \sin\left[2\pi\left(\frac{z}{\lambda} - \nu t\right) + \phi_x(t)\right] \hat{x} \\
&\quad + E_y(t) \sin\left[2\pi\left(\frac{z}{\lambda} - \nu t\right) + \phi_y(t)\right] \hat{y}.
\end{aligned}
\tag{1.1}
$$

The degree to which the additional phase terms $\phi_x(t)$ and $\phi_y(t)$ are correlated is the degree to which the light is polarized. Time-averaging over the electric field oscillations, we can describe the polarization with the Stokes parameters

$$
I \propto \langle E_x^2 \rangle + \langle E_y^2 \rangle,
\tag{1.2}
$$

$$
Q \propto \langle E_x^2 \rangle - \langle E_y^2 \rangle,
\tag{1.3}
$$

$$
U \propto \langle 2E_x E_y \cos(\phi_x - \phi_y) \rangle,
\tag{1.4}
$$

$$
V \propto \langle 2E_x E_y \sin(\phi_x - \phi_y) \rangle,
\tag{1.5}
$$
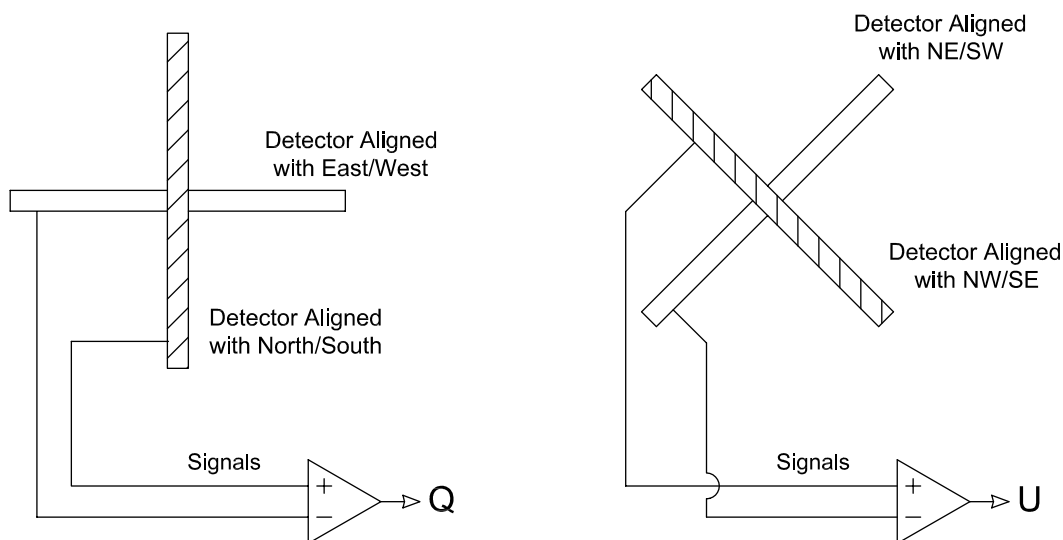
Figure 1.2: Q and U as measured by idealized polarization detectors aligned as shown.

where I refers to the intensity, Q and U describe the linear polarization and depend on the definition of the (x, y) coordinate system, and V describes the circular polarization of the photon.

The Stokes parameters are often converted from units of intensity to brightness temperature through cross-calibration with an astrophysical source of known temperature and emissivity. Equivalently, Q is defined as the temperature difference measured between two single-polarization detectors, one aligned with the North-South (N-S) direction, and the other aligned with the East-West (E-W) direction. Likewise, U can be defined as the temperature difference measured between detectors aligned with the NE-SW and NW-SE directions as shown in Figure 1.2. We will use temperature units to describe Stokes parameters throughout this thesis.

Q and U are not rotationally invariant observables, but instead transform under rotation by angle θ from coordinates (x, y) to (x', y'), following the rule

$$Q' = Q \cos 2\theta + U \sin 2\theta \qquad (1.6)$$

$$U' = -Q \sin 2\theta + U \cos 2\theta. \qquad (1.7)$$

The fractional polarization p of the photon can be defined as follows:

$$p \equiv \frac{\sqrt{Q^2 + U^2 + V^2}}{I}, \tag{1.8}$$

and the polarization angle θ_p, defined for $[0 < \theta_p < \pi]$, is

$$\theta_p \equiv \frac{1}{2} \tan^{-1}(U/Q). \tag{1.9}$$

Polarization sky maps place a line with length scaled by p at each point (θ, ϕ) on the map, at an angle θ_p with respect to a chosen coordinate system.

Further useful definitions include

$$I_x \equiv \frac{1}{2}(I + Q), \tag{1.10}$$

$$I_y \equiv \frac{1}{2}(I - Q), \tag{1.11}$$

although it is important to remember that these are not vector components of I. I_x and I_y would be the intensities measured by "perfect" single-polarization detectors oriented in the x- and y-directions. Note that $Q = I_x - I_y$ and $U = 0$, as anticipated by Eqns. 1.3 and 1.4. If the (x, y) coordinate system is rotated by 45°, $Q = 0$ and $U = I_x - I_y$, as anticipated by Eqn. 1.6.

1.3   CMB Polarization Theory

Polarization arises due to asymmetric emission, absorption, or scattering of photons. There are several astrophysical sources of polarization. For instance, elongated dust grains in star-forming regions emit or absorb light with polarization direction orthogonal to local magnetic field lines [21].

CMB polarization arises from the asymmetric Thomson scattering in the era of hydrogen combination. Significant polarization requires a sufficient number of available scatterers, but at the same time requires a low optical depth, since numerous scatters will smear out preferred polarization directions. CMB polarization is generated

during the relatively short period of time after free-streaming has begun, but before combination ends. As a result, an observed intensity distribution at the surface of last scattering (as measured by a typical CMB ΔT experiment) should be associated with a polarization pattern. The source of polarization is asymmetric temperature fluctuations of amplitude ΔT/T $\sim 10^{-5}$. The polarization level should be smaller still, with ΔQ/T $< 10^{-6}$ [30].

Consider the final scatter of a CMB photon off of a free electron and into the $\hat{z}$ direction, as shown in Figure 1.3. The scattering cross section is

$$\frac{d\sigma}{d\Omega} = \frac{3\sigma_T}{8\pi}\,|\hat{p}\cdot\hat{p}'|^2 \,\propto \cos^2\theta, \qquad (1.12)$$

where σ_T is the usual Thomson cross section to scattering, $\hat{p}'$ is the polarization direction of the incident beam, $\hat{p}$ is that of the outgoing beam, and θ is the angle formed by the two vectors [8]. The $\cos^2$ form of the cross section requires that, in order to observe nonzero linear polarization from a small source region, that region must lie within an intensity distribution $I(\theta,\phi)$ that possesses a nonzero quadrupole ($l = 2$, $m = 0, \pm 1, \pm 2$) moment [40]. This intensity distribution can arise from Doppler shifts associated with motion of the photon-baryon plasma or wavelength shifts caused by the passage of gravitational waves.

CMB temperature anisotropies are generated by both "scalar" ($m = 0$) perturbations, caused by variations in density, and "tensor" ($m = \pm 2$) perturbations, caused by primordial gravitational waves. The independent contribution of each type of perturbation can be disentangled due to their differing contributions to the resultant polarization pattern. "Vector" ($m = \pm 1$) perturbations are due to Doppler shifts associated with whirlpool motion, and are not associated with density inhomogeneities. Therefore, whatever primordial vector perturbations may have existed in the early universe would not grow with the expansion of the universe, and are not expected to be observable [30][1].

Scalar ($m = 0$) perturbations arise in the acoustic expansion and compression

---

[1]However, any CMB polarization experiment sensitive to Q and U could, in principle, detect vector-modes of polarization if they do exist.
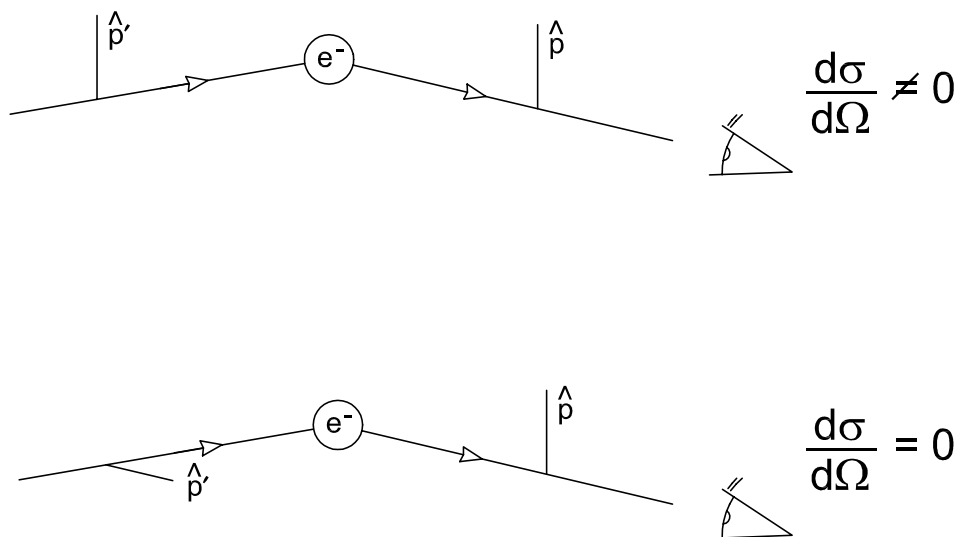
Figure 1.3: During Thomson scattering, certain orientations of incoming and outgoing polarization vectors are excluded. Eye graphic represents direction in which differential scattering cross section is measured.

of the primordial plasma. Such processes have no preferred "handedness" and, as such, can only produce polarization patterns with no curl (Figure 1.4) [30]. Direct measurement of the amplitude and distribution of scalar perturbations would represent a milestone in the study of CMB anisotropies because they would *(i)* verify that temperature anisotropies in the CMB were generated in the era of combination: any process other than reionization which altered the CMB intensity after combination would not alter the polarization, as there would no longer be sufficient numbers of charged scattering bodies; *(ii)* verify that the gravitational instability model of collapsing primordial density perturbations is correct at its earliest directly observable epoch: combination; and *(iii)* verify that the photon propagation models which relate the observed intensity distribution to a set of initial cosmological parameters are accurately representing the scattering events which occurred. In short, a measurement of scalar perturbations would firm, at very high redshift, the observational footing on which the gravitational instability paradigm rests.

Tensor ($m = \pm 2$) perturbations are associated with the passage of gravitational waves through the primordial plasma. Gravitational waves are self-propagating dis-
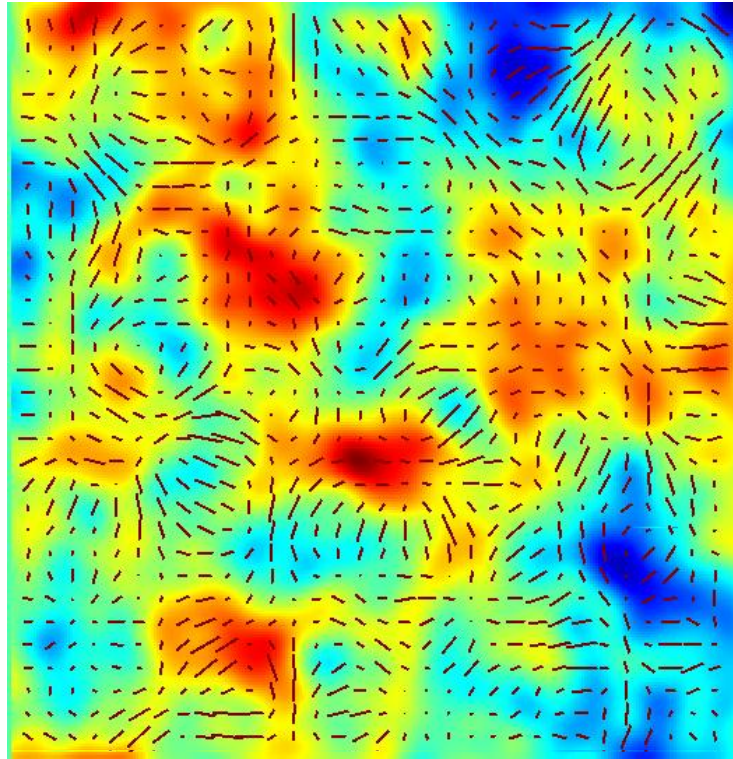
Figure 1.4: Simulated polarization G-mode pattern due to density perturbations. Note that, on these angular scales, polarization pattern is radial near hot (red) spots and tangential to cold (blue) spots. From the Ph.D. thesis of M. Zaldarriaga [81].

tortions in the space-time metric. Space in the two directions perpendicular to the direction of motion of a passing gravitational wave either contracts or expands, depending on the wave's phase – this expansion affects the wavelength of nearby photons and, therefore, their intensity. The direction of expansion rotates clockwise or counter-clockwise as the wave propagates, and so gravitational waves have a well-defined "handedness." As gravitational waves pass the surface of last scattering, they create both curl and curl-free patterns in the CMB polarization field. Direct measurement of the amplitude and distribution of tensor perturbations would represent a breakthrough in the testing of inflationary models of cosmological evolution prior to the era of combination, since these models predict primordial gravitational-wave spectra that depend on the specific form and amplitude of the potential that drives superluminal expansion [60]. Measurement of a curl component to CMB polarization may be contaminated, however, by weak gravitational lensing of the CMB in the period subsequent to last scattering [31].

1.4 CMB Polarization Angular Power Spectrum

Because of its vector nature, the formalism through which we compare measurement and theory is more complex for polarization than it is for intensity anisotropies. Since anisotropy of the CMB generates polarization, it is natural to extend the formalism for analysis of anisotropies to polarization. Maps for which the CMB temperature T is known in each direction $\hat{n}$ are routinely analyzed via expansion of the map in spherical harmonics Y_{lm}:

$$\frac{T(\hat{n})}{T_{cmb}} = 1 + \sum_{l=1}^{\infty} \sum_{m=-l}^{l} a_{lm}^T Y_{lm}(\hat{n}), \qquad (1.13)$$

where

$$a_{lm}^T = \frac{1}{T_{cmb}} \int d\hat{n} \, T(\hat{n}) Y_{lm}^*(\hat{n}), \qquad (1.14)$$

and $T_{cmb} = 2.728$ K is the average temperature of the CMB [70]. The auto-correlation function C_l^T, defined by

$$\langle a_{lm}^{T\,*}\, a_{l'm'}^{T}\rangle = C_l^T \delta_{ll'}\delta_{mm'},\tag{1.15}$$

is predicted by theory. The C_l^T's are expected to depend on such cosmological parameters as the total mass-energy density Ω of the Universe, the vacuum energy density Ω_v, the baryon density Ω_b, Hubble's constant H_0, and the slope n of the primordial power spectrum, among others. The multipole moments a_{lm}^{T} are a realization of the underlying statistical theory that are specific to our universe and our unique viewpoint within it. The expected variance in $\Delta\mathrm{T} \equiv \mathrm{T}(\hat{n})$ - T_{cmb} is

$$\langle(\Delta\mathrm{T})^2\rangle = \sum \frac{2l+1}{4\pi}C_l^T W_l\tag{1.16}$$

where W_l is a window function which takes into account the l-space sensitivity of the observing strategy.

Following Knox [39], we consider a map made of the entire sky with a Gaussian beam. The window function $W_l = e^{-l^2\theta_b^2}$, where θ_b is the Gaussian beam-width [39]. Temperature fluctuations are measured with noise per pixel σ_T. The noise in a measurement of the theory parameters C_l^T is

$$\frac{\Delta C_l^T}{C_l^T} = \sqrt{\frac{2}{2l+1}}\left(1 + \frac{4\pi\sigma_T^2}{N_p C_l^T W_l}\right),\tag{1.17}$$

where N_p is the number of independent pixels for which temperature measurements are made. Importantly, there is a fundamental lower limit to the noise

$$\left(\frac{\Delta C_l^T}{C_l^T}\right)_{min} = \sqrt{\frac{2}{2l+1}}\tag{1.18}$$

which is interpreted as "cosmic variance" and is due to the fact that, at any angular scale, there are a limited number of independent temperature measurements one can make of the sky, which is of finite solid area.

The measured temperature power spectrum associated with the BOOMERANG
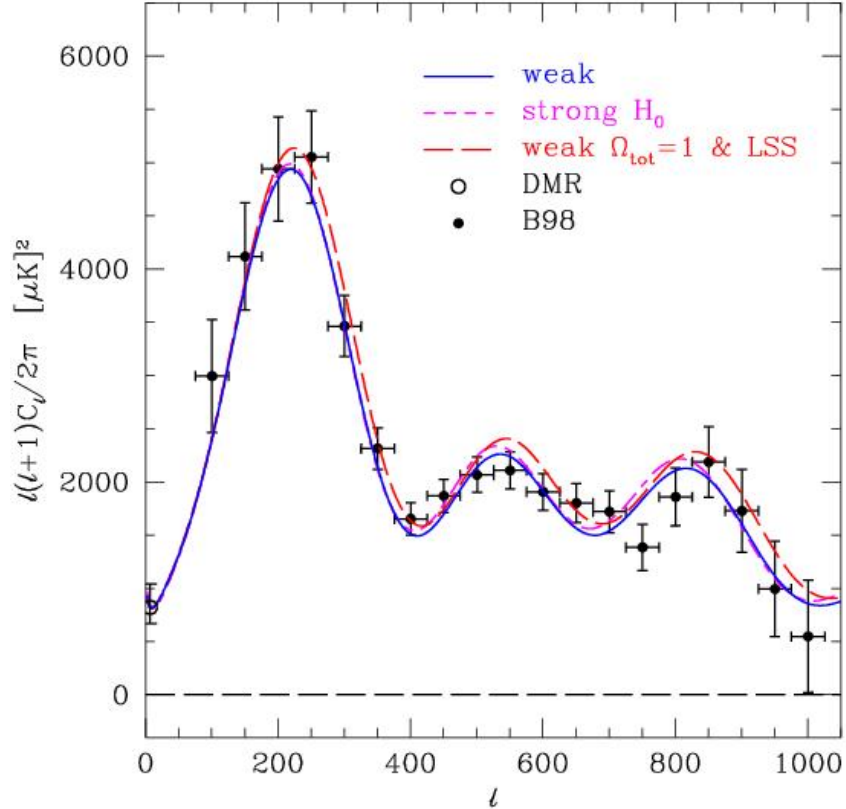
Figure 1.5: Power spectrum of cosmic microwave background fluctuations obtained by the BOOMERANG instrument in an Antarctic balloon flight in Winter of 1999/2000. BOOMERANG points are labelled 'B98.' Large angle results obtained by the COBE DMR experiment are labelled 'DMR.' Three $\Omega = 1$ CDM models are included; specific details of those models can be found in [41].

map (Figure 1.1) is included as Figure 1.5.

Kamionkowski et al. [35] have developed a formalism very similar to that described above for the analysis of polarization maps. (A separate and equivalent formalism has been developed by Zaldarriaga et al. [79]). They define a symmetric, trace-free tensor $P_{ab}(\hat{n})$ which describes the linear polarization observed in direction $\hat{n} = (\theta, \phi)$,

$$P_{ab}(\hat{n}) = \frac{1}{2} \begin{pmatrix} Q(\hat{n}) & -U(\hat{n})\sin\theta \\ -U(\hat{n})\sin\theta & -Q(\hat{n})\sin^2\theta \end{pmatrix}. \tag{1.19}$$

By analogy to (1.13), $P_{ab}(\hat{n})$ is expanded as a sum of appropriate orthonormal basis

functions on the sphere,

$$\frac{P_{ab}(\hat{n})}{T_{cmb}} = \sum_{l=1}^{\infty} \sum_{m=-l}^{l} \left[a_{lm}^G Y_{(lm)ab}^G(\hat{n}) + a_{lm}^C Y_{(lm)ab}^C(\hat{n}) \right], \tag{1.20}$$

where

$$a_{lm}^G = \frac{1}{T_{cmb}} \int d\hat{n} \, P_{ab}(\hat{n}) Y_{lm}^{G\,ab\,*}(\hat{n}), \tag{1.21}$$

$$a_{lm}^C = \frac{1}{T_{cmb}} \int d\hat{n} \, P_{ab}(\hat{n}) Y_{lm}^{C\,ab\,*}(\hat{n}), \tag{1.22}$$

and the basis functions $Y_{(lm)ab}^G$ and $Y_{(lm)ab}^C$ are covariant second derivatives on the sphere of the usual spherical harmonics Y_{lm}, chosen because they are a complete orthonormal basis set for symmetric trace-free tensors. The expansion of the polarization tensor is broken into two natural sets of basis functions, labeled G and C, since a symmetric trace-free 2×2 tensor such as P_{ab} can be written as a sum of two tensors, one with "electric" or "gradient" parity $(-1)^l$ and one with "magnetic" or "curl" parity $(-1)^{l+1}$.

The multipole moments a_{lm}^G, a_{lm}^C, and the temperature multipole moments a_{lm}^T should completely describe a map of the CMB in both temperature and polarization. An expanded set of power spectra is needed to fully characterize the temperature and polarization state of the CMB:

$$\langle a_{lm}^{T*} \, a_{l'm'}^T \rangle = C_l^T \delta_{ll'} \delta_{mm'}, \tag{1.23}$$

$$\langle a_{lm}^{T*} \, a_{l'm'}^G \rangle = C_l^{TG} \delta_{ll'} \delta_{mm'}, \tag{1.24}$$

$$\langle a_{lm}^{G*} \, a_{l'm'}^G \rangle = C_l^G \delta_{ll'} \delta_{mm'}, \tag{1.25}$$

$$\langle a_{lm}^{G*} \, a_{l'm'}^C \rangle = C_l^{GC} \delta_{ll'} \delta_{mm'}, \tag{1.26}$$

$$\langle a_{lm}^{C*} \, a_{l'm'}^C \rangle = C_l^C \delta_{ll'} \delta_{mm'}, \tag{1.27}$$

$$\langle a_{lm}^{C*} \, a_{l'm'}^T \rangle = C_l^{CT} \delta_{ll'} \delta_{mm'}. \tag{1.28}$$

If the universe prefers no overall direction for CMB polarization, C_l^{GC} and C_l^{CT} are zero by symmetry. The remaining C_l's encode fundamental cosmological parameters.

Generation of temperature anisotropies through scalar processes such as gravitational collapse will produce only G-type polarization since there is no preferred handedness or curl direction for such processes. Temperature anisotropies generated through tensor (and vector) processes such as the influence of primordial gravity waves will produce both G- and C-type polarization [35, 68]. Temperature and polarization power spectra generated by CMBFAST [12] for a given cosmological model are shown in Figure 1.6.

The reader is directed to Kamionkowski et al. [35] for an extension of this formalism which allows for the calculation of multipole moments and variances given measured polarization two-point correlation functions. In §4.6, we will apply this formalism to an observing strategy which measures CMB polarization in a ring about the north celestial pole. In analogy to Eqn. 1.16, the expected variance in total polarization $Q^2 + U^2$ is

$$\langle Q^2 + U^2 \rangle = \frac{1}{2} \left(\sum \frac{2l+1}{4\pi} C_l^G W_l + \sum \frac{2l+1}{4\pi} C_l^C W_l \right), \qquad (1.29)$$

where we've assumed that $W_l^G = W_l^C = W_l$, the window function calculated for the equivalent CMB ΔT experiment [35].

1.5 Measurements to Date

Two recent measurements provide the must stringent upper limits on the polarization angular power spectrum. At medium angular scales, Hedman et al. [24] have placed limits on C_l^G and C_l^C with a ground-based correlation polarimeter, PIQUE. To simplify the comparison of one experimental result to another, polarization measurements are often expressed in terms of "flat band power" temperatures, such that $l(l+1)C_l^X/2\pi = T_X^2$ where X refers to G- and C-type polarization. In the multipole windows $\langle l_G \rangle = 211^{+294}_{-146}$ and $\langle l_C \rangle = 212^{+229}_{-135}$ they place 95% confidence limits on the flat band power of the G- and C-type power spectra of 10 and 9 μK respectively, and a limit on the G-type spectrum of 7 μK if C_l^C is assumed to be zero. These

results have been divided by $\sqrt{2}$ to account for the difference between the G & C formalism for polarization power spectra used here and the E & B formalism used by Hedman et al. This upper limit, along with predicted angular power spectra for a chosen cosmological model, are plotted in Figure 1.6.

At large angular scales, Keating et al. [37] have placed limits on C_l^G and C_l^C with a ground-based correlation polarimeter, POLAR. In the multipole windows $l = 2$ – 20 they place 95% confidence limits on the flat band powers of the G- and C-type power spectra of 7 μK, and a limit on the G-type spectrum of 6 μK if C_l^C is assumed to be zero. Again, these results have been divided by $\sqrt{2}$ to account for the difference between the G & C formalism for polarization power spectra used here and the E & B formalism used by Keating et al.
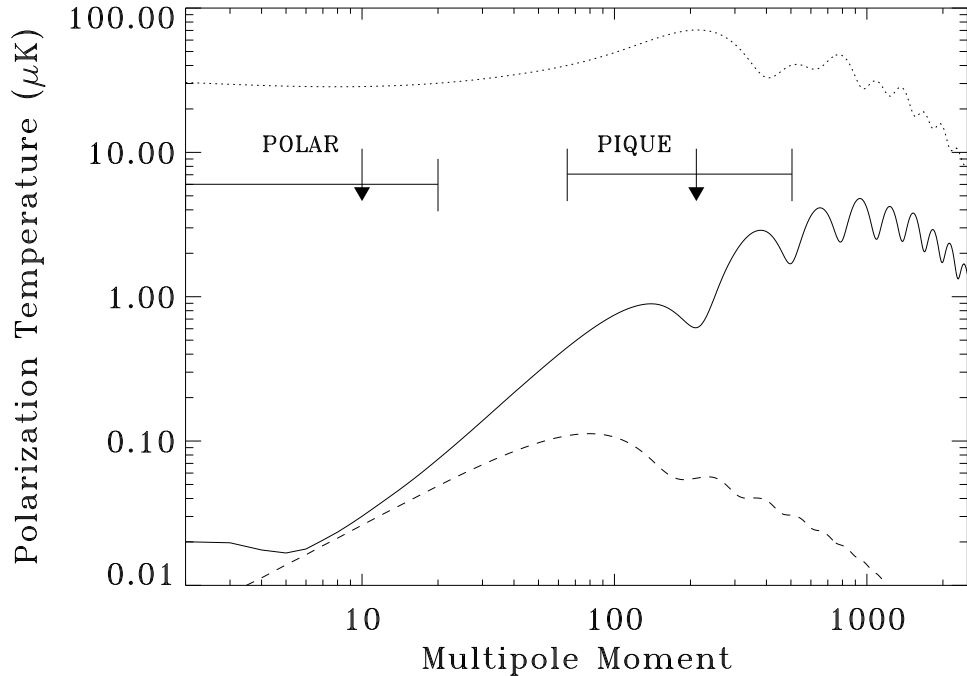
Figure 1.6: Model angular power spectra generated by CMBFAST [12] are plotted for a BOOMERANG-consistent universe with primordial scalar spectral index $n_S = 0.97$, $n_T = 1 - n_S$, and ratio of contributions to the $l = 2$ ΔT quadrupole from tensors and scalars $T/S = 7(1 - n_S) = 0.21$. Solid line is G-type polarization, dashed line is C-type polarization, and dotted line is best fit temperature power spectrum to Boomerang data. Upper limits are from the PIQUE and POLAR experiments, assuming $C_l^C = 0$, as described and referenced in text.

The Saskatoon experiment [52] put a 95% confidence upper limit of 16 μK on CMB polarization in the angular scale range corresponding to $50 \leq l \leq 100$. At smaller angular scales, $1' \leq \theta \leq 3'$, Partridge et al. [53] put a 95% confidence upper limit of 100 μK on polarization. (These data have not been reanalyzed to provide meaningful band power limits for inclusion in Figure 1.6.)

1.6 Measurements Planned

On June 30, 2001, NASA's Microwave Anisotropy Probe (MAP) began its trip to the L2 Earth-Moon Lagrange point[2]. Although it is primarily intended to measure temperature anisotropies, it also has sensitivity to polarization. ESA's Planck Surveyor, to be launched in 2007, will create full-sky maps in polarization at many frequencies[3]. The High Frequency Instrument (HFI) on the Planck Surveyor should be sensitive enough to allow polarization angular power spectroscopy.

In advance of these observatories, many projects are planned or already underway. Experimental techniques vary greatly, with significantly different detector systems (incoherent, coherent correlation, and coherent Dicke-switched polarimeters), polarization analyzers (orthomode transducers, wire grids, polarization-sensitive bolometers, and wave plates), observing frequencies (between 15 and 400 GHz), telescopes (upward-looking horns, single on- and off-axis dishes, and interferometers), beam sizes (from 7° to 2.5'), observing sites (balloon- and satellite-borne as well as ground-based), and scan strategies (switched, scanned, and drift-scanned; observations of rings, patches, or the entire sky). For a review of some current polarization experiments, see Staggs et al. [72].

In particular, the University of Chicago-based Degree Angular Scale Interferometer (DASI)[4], promises high sensitivity to CMB polarization from its location at the South Pole. DASI recently completed a survey of intermediate angular scale CMB ΔT fluctuations [62, 22, 45] and was reconfigured for polarization observations in

---

[2] *http://map.gsfc.nasa.gov*
[3] *http://astro.estec.esa.nl/SA-general/Projects/Planck*
[4] *http://astro.uchicago.edu/dasi/*

Winter 00/01. Observations were made over the recent austral winter, and analysis of the polarization data is ongoing. The complementary Caltech-based Cosmic Background Imager (CBI)[5] measured small angular scale ΔT fluctuations [55], and has been reconfigured for polarization observations from its site on the Atacama Plateau in Chile [7].

1.7 Observing Strategies

For any CMB polarization experiment, the instrument design aims to utilize available experimental resources to maximize the polarization signal of interest while minimizing sources of statistical and systematic error.

Choice of observing frequency is as critical to CMB polarization experiments as it is to CMB ΔT experiments, with the complication that some polarization analyzers (such as half-wave plates) are fundamentally chromatic. Ground-based observatories must contend with atmospheric emission and absorption, which is a strong function of wavelength. Moving to longer wavelengths reduces background detector loading from sky temperature, but increases sensitivity to galactic synchrotron emission, which can be highly polarized. Due to the unknown distribution of galactic foreground emission, especially polarized emission, multi-frequency experiments are preferable. However, multi-frequency, multi-pixel focal planes require off-axis pixels. Off-axis reflections will introduce polarization offsets which may vary with observing conditions or pointing direction. Observational strategies based on sequential observations with different spectral bands suffer due to the long integration times which will be required to observe polarization signal at any single frequency.

Instrument beam-size is determined primarily by the scientific goal of the experiment. The macroscopic wavelengths of CMB radiation ($\lambda_{peak} \sim 1$ mm) mean that realistically sized optical systems produce large diffraction-limited beams ($\theta \sim \lambda/D_{tel}$), especially at long wavelengths. Since polarization signals must be causally generated at the surface of last scattering, the angular scales of interest are at or below the

---

[5]*http://www.astro.caltech.edu/ tjp/CBI/*

horizon size at the time of scattering. Large-angular scale polarization ($l \sim 20$), potentially generated at a late last scattering during reionization, can be observed with large feed horns directly. Small-angular scale polarization ($l \sim 500$), generated in the era of combination, must be observed with telescopes with large collecting area.

Radio-wavelength detectors have traditionally detected a single-polarization by making use of waveguide polarization analyzers such as orthomode transducers to separate the two senses of linear polarization. Half-wave plates have been utilized to modulate the incoming polarization pattern. Alternative polarization analysis schemes utilize wire grids or polarization sensitive detectors to analyze the polarization of two separate beams. For instance, two concentrating feeds can illuminate a large wire grid positioned at a $45°$ angle with respect to incoming radiation. The rejection of common mode signal in that case would depend on how well the two separate beams can be aligned on the sky. The quality of polarization analysis provided by side-by-side single-polarization detectors of varying orientation will depend on the stability of the differing side-lobe and off-axis optical responses of the two detectors. Polarization sensitive bolometers will soon provide an attractive way to measure both senses of linear polarization in a single beam, utilizing a compact feed structure [34].

Choice of observing platform and detector system will ultimately determine the amount of integration time necessary to make a statistically significant detection of polarization. The South Pole, Mauna Kea, the Atacama plateau in Chile, and balloon altitudes are attractive observing locations due to the low column density of water vapor. CMB polarization measurements, however, are subject to potential systematic effects which have never before been encountered, not even in typical millimeter-wavelength measurements of polarized emission from galactic and extragalactic sources. Some teams have chosen to forgo premium observing conditions in exchange for the thorough understanding of polarization systematics that instrumental accessibility provides. Ground- and balloon-borne measurements in the coming years will lay the groundwork for a dedicated, spacecraft-borne instrument capable of probing the gravitational-wave contribution to CMB polarization.

Chapter 2   Polatron Receiver

In this chapter, we introduce and describe the Polatron, a CMB polarimeter. Specific emphasis is placed on the optical design of the telescope and receiver. Detailed discussion of the cryogenic system is deferred to the next chapter.

2.1   Introduction

The Polatron is designed to be used at the 5.5 m telescope at the Owens Valley Radio Observatory (OVRO) to measure CMB polarization on angular scales where the signal is expected to be highest, and in a spectral band where galactic foregrounds are expected to be lowest. The radiometer shares many elements of design with the SuZIE [29] and Boomerang [16] experiments and with ESA's Planck Surveyor. A single entrance feed is coupled to an orthomode transducer (OMT), which efficiently separates the two states of linear polarization. Each OMT output is spectrally filtered and then terminated in a silicon-nitride micromesh bolometer. The bolometer signals are electronically differenced, producing a signal that is proportional to the difference in optical power in the two arms of the OMT. A half-wave plate placed in front of the receiver continuously rotates the incoming plane of polarization, allowing us to alternate between measurements of Q and U at a modulation frequency we choose. This provides a strong check on systematic errors. The detectors are cooled to 0.25 K by a combination of a closed-cycle mechanical cryocooler and a closed-cycle three-stage helium sorption cooler. A synopsis of the experimental specifications can be found in Table 2.1. A schematic of the polarimeter is included as Figure 2.1.
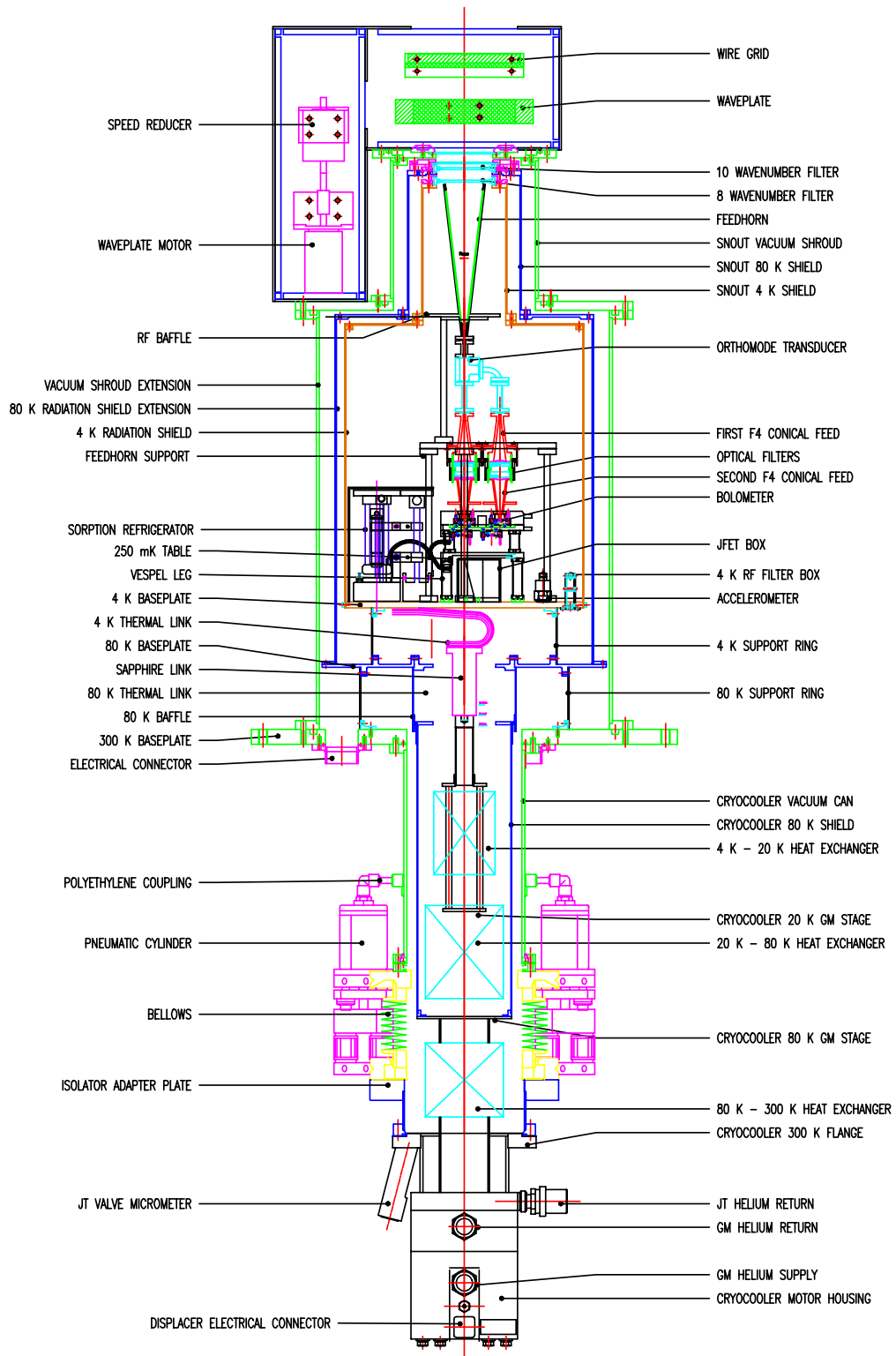
Figure 2.1: Polatron General Assembly.

Telescope:	5.5 m Cassegrain Focus
Polarization Analysis:	Rotating Wave Plate and Orthomode Transducer
Polarization Efficiency:	$> 95\%$
Spectral Band:	$88 - 106$ GHz
Beam Size:	2.5 arcminutes FWHM
Detectors:	Silicon-Nitride Micromesh Bolometers
Sensitivity:	$\sim 500\ \mu$K s$^{1/2}$ to Q and U

Table 2.1: Receiver Specifications

2.2 Telescope

The design of the Polatron optics aims to minimize background loading and systematic polarization effects while efficiently coupling the detectors to the sky with a beam matched to angular scales of scientific interest. The OVRO 5.5 m telescope (Figure 2.2) is ideally suited for such observation. From 1992 to 1997, this telescope was dedicated to measurements of primary and secondary CMB anisotropies as described in Herbig et al., Myers et al., Leitch et al., and Mason et al. [25, 51, 44, 48]. As part of this program, the telescope was modified to minimize the warm ground emission that couples into the receiver by scattering from the secondary mirror support legs, resulting in a measured ground spillover temperature of 9 K [42].

The telescope has never before been used at wavelengths < 1 cm. Although the surface is sufficiently smooth on wavelength scales, large-scale dish deformities might distort and/or dilute our beam. The dish consists of 16 panels, each of which is deformable and supported in nine places with bolts and calibrated brass shims (Figure 2.3). By altering the phase front distribution of the beam at the dish surface, a gaussian distribution of surface deformities described by an rms deviation δ_{dish} from

Figure 2.2: A photo of the OVRO 5.5m telescope.

parabolic scatters power out of the main beam. The Ruze equation [67] relates the loss in point source gain g for observations at wavelength λ for such perturbations:

$$g = e^{-(2\pi\delta_{dish}/\lambda)^2}. \tag{2.1}$$

When the telescope was assembled at its original Table Mountain site, the surface was measured and set to 0.20 mm *rms* accuracy. When the telescope was later disassembled and moved to the Owens Valley, the shim thicknesses were recorded and reproduced, but upon reassembly no new surface measurement was made. In February, 1999, we measured the shape of the dish with an array of high-resolution AC-biased capacitive sensors mounted on a rotating parabolic arm. A thorough discussion of this campaign can be found in [69]. On ≥ 10 cm length scales, the measured surface *rms* accuracy was 0.24 ± 0.02 mm or $\sim \lambda/13$ for $\lambda = 3$ mm. Removal and addition of shims under the surface allowed us to reduce the *rms* surface accuracy

Figure 2.3: Surface setting campaign. Top left: photo taken during installation of a previously unused panel. Top right: reattachment of panel to telescope support after shim thickness had been changed. Bottom: close-up of the measurement arm and capacitive sensors; panel in photo was later replaced.

to 0.15 ± 0.02 mm or $\sim \lambda/20$ (Figure 2.4).

Upon reflection off a metal surface, unpolarized light becomes partially polarized in a direction along the reflecting surface [23]. For the type of off-axis telescopes favored for low-background CMB ΔT measurements, large polarization offsets arise which may depend on pointing direction and dish temperature. In order to minimize the number of reflections, particularly off-axis reflections, the Polatron receiver beam waist will be placed directly at the Cassegrain focus of the telescope, which lies 45.7 cm *above* the parabolic surface. A single entrance feed illuminates the primary mirror.
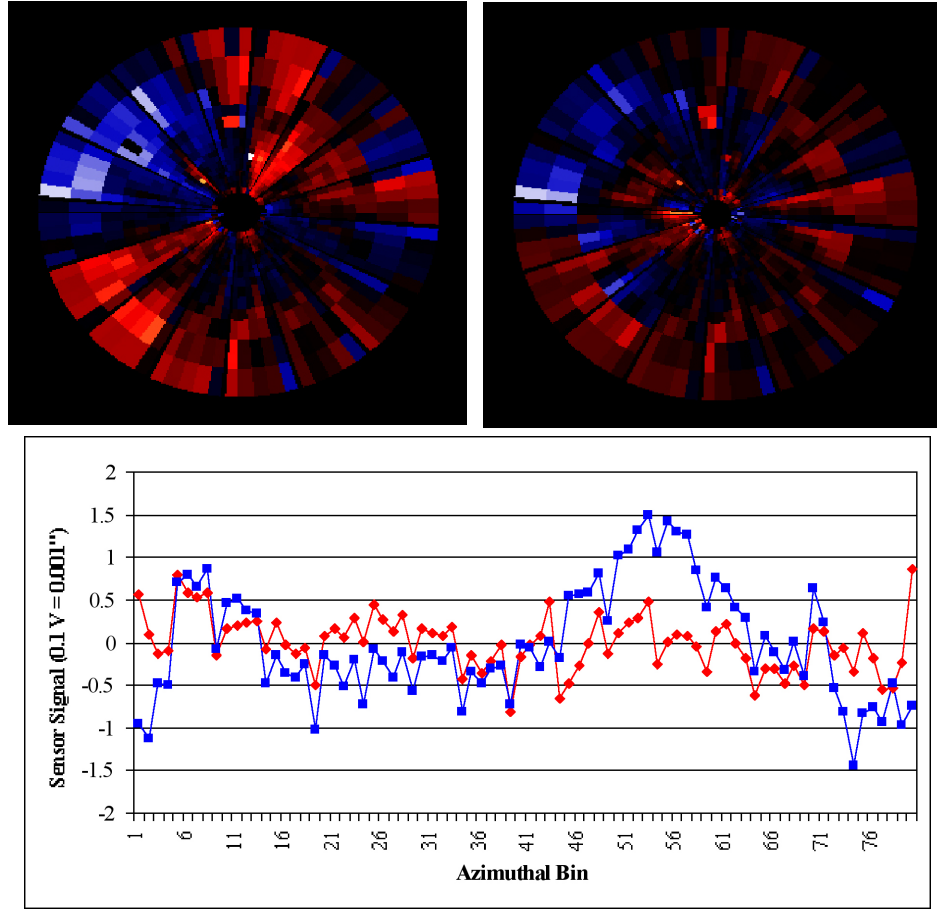
Figure 2.4: Surface setting campaign. Top left: image of surface height fluctuations made by measurement arm before improvements were made. Top right: image of same, after improvements. Bottom: plot of surface height fluctuations as a function of azimuth angle at a fixed radius; blue is before, red is after improvements. Azimuthal bin number one corresponds to north in the polar maps.

2.3   Waveplate

In front of the entrance feed is placed a rotating, ambient temperature, birefringent, crystalline quartz half-wave plate[1] 7.6 cm in diameter and 3.26 cm thick. The wave plate generates a π phase retardation between electric field vectors with wavelength ~ 3 mm incident on the fast and slow refraction axes of the quartz. Consequently, the polarization pattern from the sky is reflected about the optic axis, resulting in modulation of the polarization signal at four times the physical rotation rate of the

---

[1]Valpey-Fisher Corporation, 75 South Street, Hopkinton MA 01748

wave plate. This modulation technique is employed routinely in millimeter-wave polarimetry as it allows both Stokes parameters Q and U to be measured with a single horn [21, 49].

The *polarization efficiency* of an optical element is the degree to which a 100% polarized signal will remain polarized on passage through the element. Two effects are expected to reduce the polarization efficiency of the wave plate. First, observations are made over a broad spectral band, while the wave plate is fundamentally chromatic. Second, the optics of the telescope are moderately fast, $f/3.2$. Different parts of our beam travel different path lengths through the quartz, so a phase retardation other than π will result for those parts of the beam. In order to mitigate this second effect, the wave plate is placed in the near field of the entrance feed, where the beam is most collimated. One can calculate the extent to which an input polarized signal from the sky will be depolarized by these two effects. In this system such a calculation predicts approximately 98% polarization efficiency (see Appendix A). This efficiency effect can be measured and corrected for with greater accuracy than our anticipated overall calibration uncertainty, and is different from the sources of systematic polarization discussed later.

2.4 Focal Plane

The focal plane feed structure we employ is a modification of a design [11] used by BOOMERANG, MAXIMA, and ACBAR [66], and baselined for use on the Planck HFI. Figure 2.5 is a cartoon diagram of the Polatron feed structure, illustrating the important waveguide and concentrating components. The design was driven by several concerns; in the subsections below, we itemize these concerns and discuss how each was addressed in the design.

2.4.1 Thermal Mass and Profile

Design of focal planes for telescopes with limited fields of view requires close-packing of several narrow-profile feeds. Although the Polatron is a single-pixel experiment,
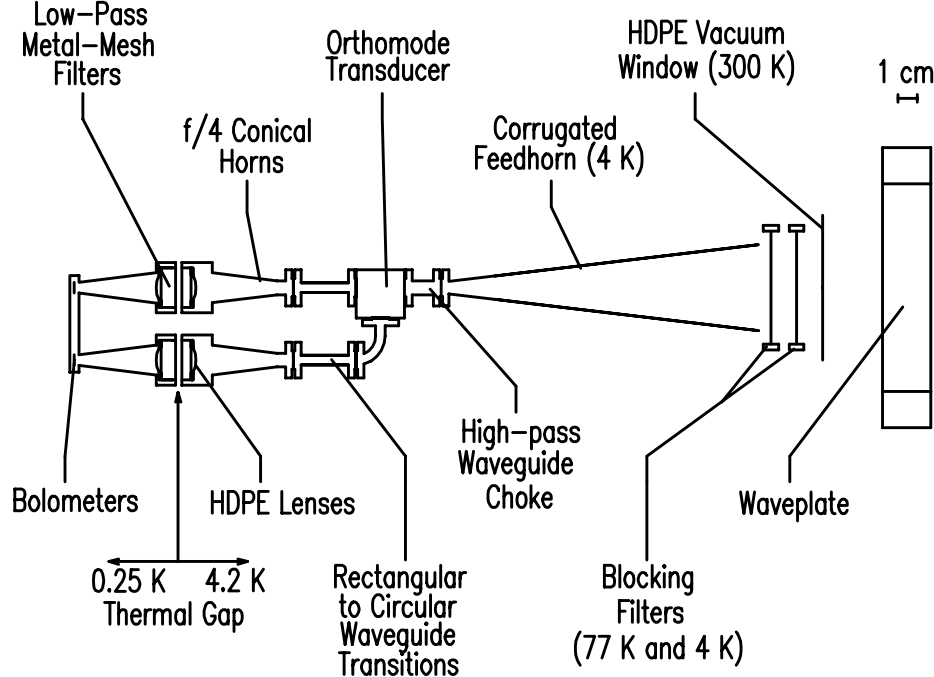
Figure 2.5: Cartoon diagram of the Polatron optical feed structure, blocking filters, and ambient temperature half-wave plate.

the position of the 5.5m telescope focus above the surface of the telescope limits the girth of the experiment as a whole. There is no equivalent limit to the length of the feed. A 90° waveguide bend in the "side-" or "off-" channel allows us to maintain a slim profile without degrading the off-channel gain. Due to the $f/3.2$ optical design of the telescope, the entrance feed is quite large: 4.1 cm in aperture diameter and 16.3 cm in length.

In order to limit the radiative load on our detectors, all components in the feed structure must be cooled to cryogenic temperatures. The limited cooling powers of the mechanical cryocooler and helium sorption cooler require minimization of the heat capacity of the entire structure. To that end, all components are machined or electro-formed from oxygen-free high-conductivity (OFHC) Cu. In addition, all components are light-weighted to the extent that such efforts do not compromise strength.

2.4.2 Polarization Analysis

Fluctuations in atmospheric emission are an important factor in the degradation of sensitivity of ground-based millimeter-wave CMB experiments. Rejection of common-mode signal between two polarization channels allows ground-based polarimeters to achieve high sensitivity. Our atmospheric model detailed in §4.2.4, suggests that a common-mode rejection ratio (CMRR) greater than 100 should effectively eliminate the contribution to total receiver noise from atmospheric 1/f noise. This corresponds to a matching between polarization states of $< 1\%$, or a systematic receiver polarization of $< 1\%$. To achieve this, a waveguide choke joins the entrance feed to an ortho-mode transducer. The ortho-mode transducer analyzes the polarization while a half-wave plate modulates both senses of incoming polarization within a single beam (§4.2).

2.4.3 Beam Response

Excellent predictive control of the beam response $g(\Omega)$ in both polarization planes is required. The waveguide choke sets the number of modes in the Gaussian decomposition of the beam response to unity. The entrance feed is corrugated, which limits the side-lobe response and improves the polarization matching. (See [56, 18, 54] for thorough discussions of the angular and polarization response of single-mode corrugated feeds.) Expressing the beam response in time-reverse as an equivalent broadcast beam, the amplitude of the electric field vector is of Gaussian form with beam width $w(z)$ such that

$$w(z) = w_0 \left[1 + \left(\frac{\lambda z}{\pi w_0^2} \right)^2 \right]^{1/2} \tag{2.2}$$

where the beam waist

$$w_0 = w_a \left[1 + \left(\frac{\pi w_a^2}{\lambda L} \right)^2 \right]^{1/2} \tag{2.3}$$

and the aperture waist $w_a = 0.6435a$ for a corrugated feed horn of aperture a and length L (the equivalent aperture waist for a smooth-walled feed horn is $0.7680a$).

The beam waist is placed at the focus of the telescope and is at a distance d_o from the horn aperture, where

$$d_0 = \frac{L}{1 + \left(\frac{\lambda L}{\pi w_a^2}\right)^2}. \tag{2.4}$$

These expressions allow us to calculate the response of the beam at the edge of the telescope primary. The horn aperture a and length L, along with the throughput-limiting waveguide choke, completely determine the primary illumination pattern. By reducing the edge response to –20 dB off maximum, we can reduce expected emission from ground spillover to < 5 K. The calculated beam width in the far field is 2.5 arcminutes.

2.4.4 Spectral Response

Bolometers are sensitive to radiation over a broad range of frequencies. The Polatron is a ground-based experiment, so detector response must be strictly limited to within available windows in atmospheric transmission. To limit off-axis reflections, we chose to use a single on-axis feed. This, coupled with the decision to use a chromatic wave plate, motivated our choice of a single observing frequency near the minimum in spectral foregrounds (§4.5). We have chosen a 20% FWHM spectral bandpass centered on 96 GHz between the 60 and 118 GHz molecular oxygen lines (Figure 5.2). Due to the faintness of the polarization signal, high efficiency (> 20%) in-band spectral filtering is desirable.

The 88 GHz low-frequency edge of our band is set by a > 3λ length of waveguide at the exit aperture of the feed horn. It is difficult to match the corrugated throat of the entrance feed to such a small diameter, so the exit aperture of the feed is smoothly reduced to the choke diameter. The 106 GHz high-frequency edge of our band is set by a metal-mesh resonant grid filter [43].

The filters are more efficient in free space than in waveguide, so we couple the outputs of the OMT to the grid filters via rectangular-to-circular waveguide transitions and $f/4$ conical feedhorns. A reciprocal $f/4$ conical feedhorn for each channel reconcentrates the radiation into tuned integrating cavities containing the bolome-

ters. High density polyethylene (HDPE) lenses at the large aperture of each $f/4$ feed collimate the radiation for passage through the filter at low incidence angle and also ensure that the two feeds couple efficiently [11]. The gap between the two $f/4$ feeds also allows us to cool the majority of the focal plane to 4 K while the bolometer back-end is cooled to 0.25 K; a similar thermal gap in waveguide would present optical alignment difficulties. The bulk of incident out-of-band optical power can be intercepted at 4 K, where more cooling power is available than at sub-Kelvin temperatures.

The metal-mesh filters were designed and fabricated at Peter Ade's laboratory in QMW College in England (the lab has since moved to the University at Cardiff.) The manufacturing process sandwiches several layers of inductive or capacitive copper mesh embedded in polypropylene sheets [43]. The filters typically exhibit a < -20 dB leak at twice their edge cut-off frequency, so an additional metal-mesh filter with an edge at 160 GHz is included. A further low-pass alkali-halide filter coated with black polypropylene blocks radiation above 1650 GHz. Both of these filters are cooled to 4.2 K. Large diameter low-pass metal-mesh filters with edges at 240 and 300 GHz are placed in front of the feedhorn, at 77 K and 4.2 K, in order to limit the thermal load from the entrance window on the band-defining filters and the cryogenic stages. The entrance window itself is a piece of HDPE with thickness tuned to minimize reflective loss in-band.

The edge filters are cooled to 4 K and 0.25 K in order to limit the radiative load on the detectors. As a result, one possible source of systematic error is long time-constant heating or cooling of these filters. In order to avoid slow drifts in detector responsivity, the filters must be well heat-sunk at 4 K and 0.25 K. To that end, we use Cu-Be wave washers to press the filters firmly against the feed structure at cryogenic temperatures.

None of the spectral filters is expected to produce significant ($> 5\%$) crosspolarization of incoming signals [1]. However, the polarization properties of the band-defining filters are immaterial, since the two polarization components of the incoming radiation have already been separated by the OMT. Systematic polarization induced by

the two blocking filters and window in front of the feed horn will remain fixed with respect to the instrument while the polarization pattern from the sky rotates with the wave plate. This effect is removed upon demodulation of our signal at four times the wave plate rotation frequency.

2.4.5 RFI Control

Instrumental sensitivity can be degraded by detector response to radio-frequency interference (RFI), which may enter through the instrument window or be generated within the experiment by the cryocooler motor. The detectors can couple to RFI radiatively, or along the length of high-impedance wiring between the detectors and their cold amplifiers. A Faraday cage formed by the 4 K radiation shield and a firewall built at 4 K isolate the susceptible components from the sources of RFI. A further advantage of the thermal break between the 4 K and 0.25 K sections of the feed structure is that the 4 K feed can be integrated with the snout of the 4 K radiation shield. Any radiation which passes through the instrument window must pass through the entrance feed – and through cold filtering – in order to couple radiatively to the detectors and cold wiring.

2.4.6 Commercial Parts

Availability and expense of existing commercial waveguide parts are balanced against the effort and expense involved in in-house design and manufacturing. The OMT and rectangular-to-circular waveguide transitions were purchased from Gamma-F Inc.[2], which supplied identical 90 GHz OMTs for the MAP observatory. An earlier, in-house design [9], manufactured by Hi-Tech Microwave[3], was rejected after its initial performance was degraded by uncontrollable slippage of the thin waveguide septum which split the two senses of polarization. The waveguide choke was designed in-house and manufactured by Zen Machining[4]. The feed horn was designed in-house

---

[2]Gamma-F Corporation, 3111 Fijita St., Torrance, CA 90505
[3]Hi-Tech Microwave, Inc., 7511 Sears Blvd., Pensacola, FL 32514
[4]Zen Machine & Scientific Instrument, 1568 Steamboat Valley Road, P.O. Box 1658, Lyons, CO
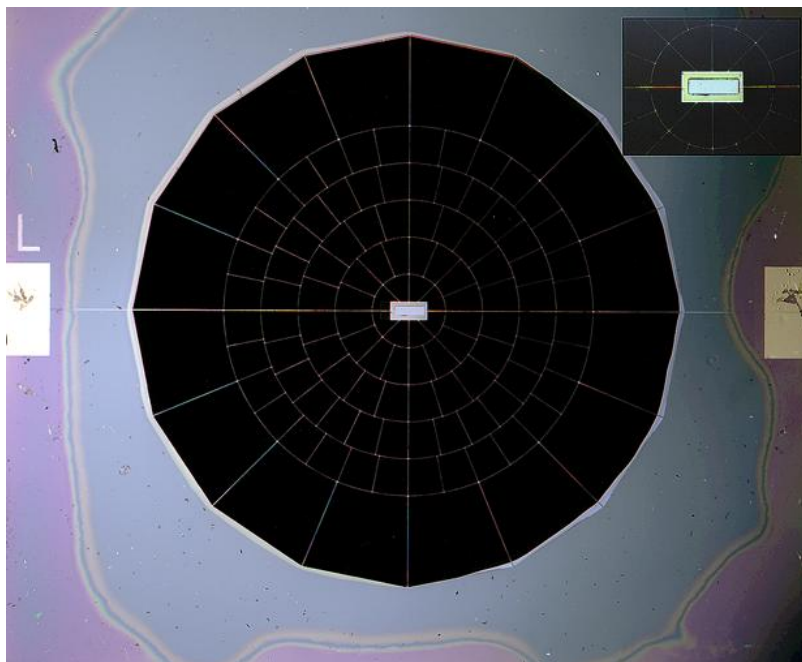
Figure 2.6: Photo of a silicon-nitride micromesh bolometer.

and electroformed by Hi-Tech Microwave. The backend feed structures were designed in-house and fabricated by the Caltech Physics Department Machine Shop.

2.4.7 Detectors

The Polatron uses two silicon-nitride micromesh ("spider-web") bolometers (Figure 2.6) supplied by the Micro-Devices Laboratory at the Jet Propulsion Laboratory. Bolometers consist of an absorber and thermistor pair suspended with thermal conductivity G from a cold bath, as shown in Figure 2.7. The impedance of the absorber determines the optical efficiency, and is controlled by depositing a thin gold film upon the absorber mesh. At the center of the absorber is an NTD Ge resistive chip with temperature-dependent resistance

$$\mathrm{R}(\mathrm{T}_{bolo}) = \mathrm{R}_0 e^{\sqrt{\Delta/\mathrm{T}_{bolo}}} \tag{2.5}$$

Incoming Light (P_{opt})

Thermistor (T_{bolo}) Conductivity (G)

Absorber

Heat Capacity (C)

Thermal Bath (T_{bath})
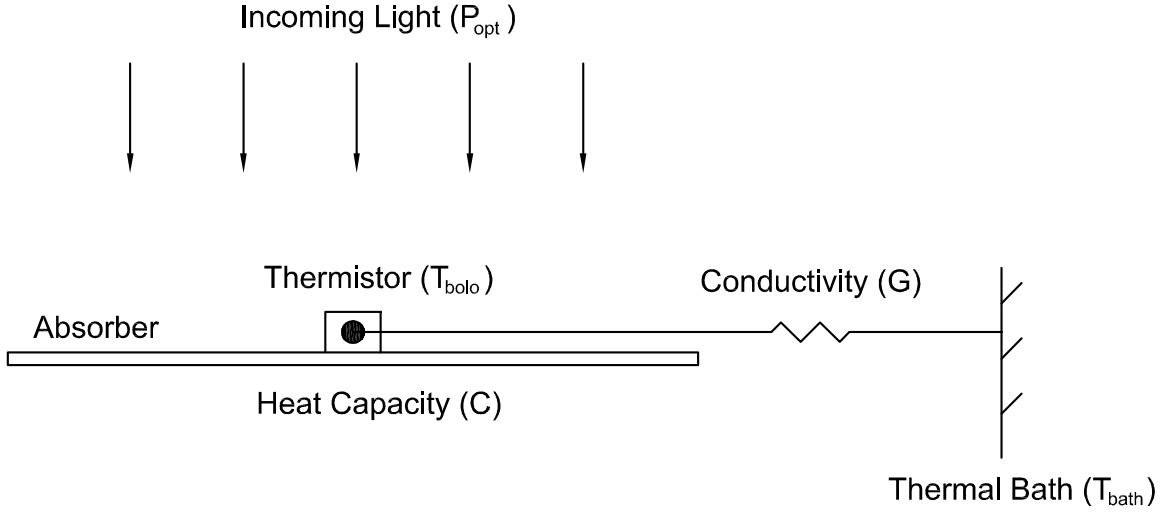
Figure 2.7: Bolometer Thermal Schematic.

where Δ and R_0 are selectable quantities, depending only on chip material and size. The thermal conductivity is chosen so that

$$G \sim \frac{P_{opt}}{T_{bolo} - T_{bath}}, \tag{2.6}$$

and T_{bolo} is not so high that the bolometer sensitivity (§4.2) and responsivity are adversely affected. The response time of the bolometer τ to a fluctuation in input power is

$$\tau \sim \frac{C}{G}, \tag{2.7}$$

where C is the heat capacity of the bolometer, typically dominated by the thermistor. The responsivity S of the system, measured in V/W, is the change in output voltage which occurs upon a change in input power. The electrical responsivity is measured by varying the input bias voltage, so that power V_{bolo}^2/R_{bolo} is dissipated in the detector, and measuring the change in output voltage. The responsivity depends on the thermistor temperature, and hence the dissipated power, so the bolometer is only linear over a small range.

The open mesh geometry of "spider-web" absorbers (i) reduces the heat capacity and, therefore, the response time of the detector; (ii) reduces the probability

Expected Optical Load P_{opt} :	3 pW per channel
Sink Temperature T_{sink} :	0.25 K
Operating Temperature T_{bolo} :	0.45 K
Thermal conductivity G :	40 pW / K @ 0.25 K
Thermistor Heat Capacity C :	1.5 pJ / K @ 0.25 K
Time Constant τ :	25 ms
Thermistor Resistance R_{bolo} :	2.0 MΩ
Noise Equivalent Power :	2.9 $\times 10^{-17}$ W Hz$^{-1/2}$
Electrical Responsivity :	3 $\times 10^8$ V/W

Table 2.2: Bolometer Specifications

of interaction with cosmic-rays; and (*iii*) reduces the detector mass and hence its susceptibility to microphonic stimulation.

Fabrication technology has improved to the point that very specific requests can be made of the thermal and electrical performance of the detectors. Selection of proper bolometer specifications under a given optical heat load amounts to maximization of the anticipated responsivity of the detectors, so that all sources of photon noise swamp the readout electronics noise, while minimizing the anticipated detector noise (§4.2). This is achieved by prudent selection of absorber and thermistor material and geometry, as well as lead conductivity. The Polatron detector specifications are listed in Table 2.2.

The 0.25 K operating temperature of the bolometers is provided by a triple-stage ^{4}He/^{3}He/^{3}He sorption refrigerator (§3). The ^{4}He stage condensation point temperature is set by an HS-4 4.2 K cryocooler purchased from APD Cryogenics[5]. A study carried out by Bhatia et al. of the susceptibility of bolometer systems to

---

[5]APD Cryogenics Inc., 1030 E. Duane Ave., Suite I, Sunnyvale, CA 94086
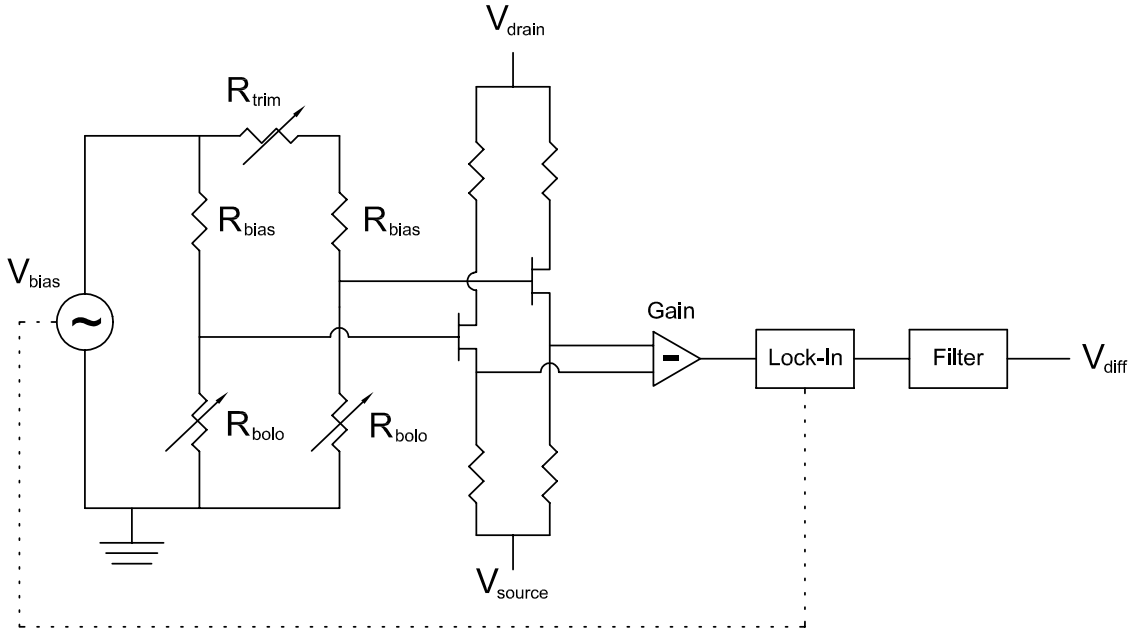
Figure 2.8: Diagram of the AC-biased bolometer readout circuit.

cryocooler microphonics suggests that cryocoolers are a feasible alternative to liquid He dewars for remote observations (§3 and [5]).

2.5   Readout Electronics

A schematic of the readout circuit is shown in Figure 2.8. The bolometers are placed in an AC-bridge and sine-wave biased at 200 Hz [77]. The relative bias levels can be adjusted to trim out gain mismatch between the two channels [28]. The output signals are buffered by a matched, 120 K, low-noise JFET pair, then differenced and demodulated in ambient temperature, low-noise amplifier electronics, producing a signal V_{DIFF} proportional to the difference in optical power in the two polarizations:

$$V_{\mathrm{DIFF}} = S_T \times \eta_{opt}\eta_{pol}\left[Q\cos(2\pi \times 4f_{wp}\,t) + U\sin(2\pi \times 4f_{wp}\,t)\right] + V_{noise}. \quad (2.8)$$

Here, S_T, measured in V/K, is the detector responsivity to thermal fluctuations; η_{opt} is the band-averaged optical (photon) efficiency of the instrument; η_{pol} is the

polarization efficiency; Q and U are measured in K, fixed to the sky, and convolved with our beam response; $f_{wp} \sim 0.6$ Hz is the physical rotation rate of the wave plate; and V_{noise} is the sum of detector noise and noise from the JFET amplifiers.

In addition to the differential measurement, the signal level of each independent bolometer is sampled and recorded. The absolute signal levels are dependent on optical loading, and so are expected to vary greatly with atmospheric conditions. As a result, the single-channel measurements are AC-coupled, with a high-pass filter cutoff at 0.06 Hz, a factor of 10 below the signal frequency. The single-channel levels may also allow us to continuously monitor the responsivity of the system: the half wave plate should produce slight differential emission between its two refraction axes, modulated at $2f_{wp}$.

An additional two bolometers with the same thermal and electrical properties and amplifier chain, but which are not exposed to light, are included in the system. These diagnostic or "dark" bolometers are a useful tool for investigation of a number of systematic effects that could impair our measurement, such as bolometer sink temperature drifts and microphonic response. All channels are low-pass filtered at 6 Hz, a factor of $\sim \pi$ beneath the bolometer frequency response limit.

All cold signals in the Polatron are carried by twisted-pair, shielded, stainless steel (TPSS) wire. Such wire is very low conductivity (G $\sim$ $10^{-3}T^{0.92}$ W cm^{-1} K^{-1} at 4 K [20]), limiting the parasitic heat load on the mechanical cryocooler and multistage cooler. The shields provide physical protection as well as protection from electromagnetic pickup. The two main disadvantages of TPSS wire are high capacitance ($\sim$ 1 pF/cm) and the time and expense involved in applying acid flux and soldering the small, low conductivity leads.

2.6   RFI Control

Electromagnetic noise sources include motors, electronic equipment, and radio and radar broadcasts. Typical frequencies of concern are in the radio portion of the spectrum: $\nu = 100$ MHz – 10 GHz ($\lambda = 3$ cm – 3 m). Lower frequencies are excluded

by the physical size of the metal exterior of our instrument, while higher frequencies are "optical" and can be controlled by spectral filters and blackened and/or reflective surfaces. Radio-frequency interference (RFI) couples to the detectors primarily through the high-impedance wiring between the detectors and cold JFET amplifiers. As discussed in §2.4.5 above, the 4 K radiation shield acts as a Faraday cage with a single aperture in the entrance feed horn. All wires running to the 4 K stage are filtered at a fire wall built into the 4 K cage.

A detailed description of the development and testing of compact cold filters for the Polatron can be found in [46]. Compact, surface mount EMI filters supplied by Murata, Inc.[6], provide an attractive < -20 dB of signal attenuation between 10 MHz and 200 MHz and < -40 dB between 200 MHz and 1 GHz, at room temperature. However, since numerous thermometry and signal lines run into the 4 K space, close-packing of these filters is required (Figure 2.9). Such packaging led to a degradation in performance due to crosstalk between adjacent filter lines, which complicated the transmission circuit. Further degradation occurred upon cooling of the filters to 4 K. Ultimately, the filters perform best between 200 MHz and 8 GHz, with measured < -20 dB attenuation across that band, in the Polatron configuration. Further RFI reduction is accomplished by potting of the entire filter and a length of lead wires in Eccosorb.

2.7 Data Acquisition System

Signal sampling is triggered by an opto-interrupter which is switched by a 64-tooth wheel physically attached to the wave plate. As a result, the sampled data is stored in a coordinate system fixed to the wave plate position, rather than as a time stream, simplifying data analysis. For a physical wave plate rotation rate $f_{wp} \sim 0.15$ Hz, this allows us to sample the bolometers at ~ 20 Hz, well above the signal frequency at $4f_{wp} = 0.6$ Hz and a factor of several above a detector bandwidth-defining low-pass filter at 6 Hz. The signal frequency 0.6 Hz also lies well above the ~ 30 mHz $1/f$ knee

---

[6]Supplied by Newark, 9630 Norwalk Blvd., Santa Fe Springs, CA 90670-2932
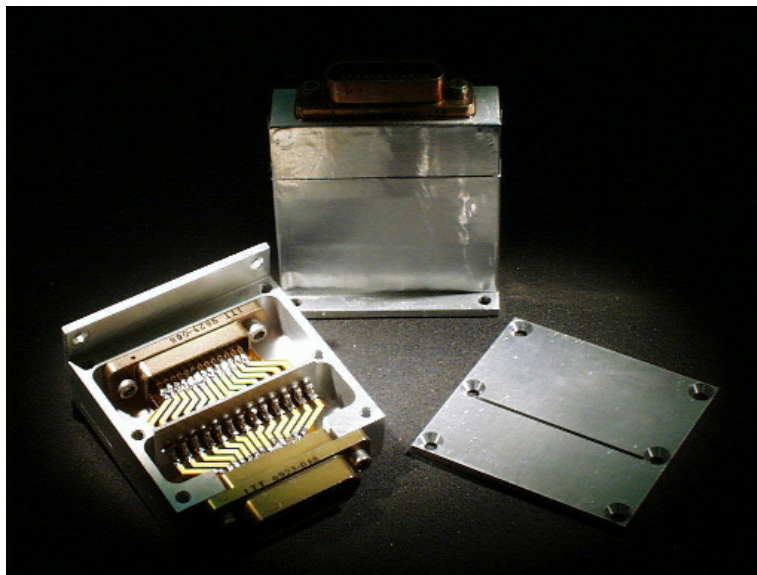
Figure 2.9: Close-packed array of RFI filters.

of the readout electronics (see Table 2.3 for a synopsis of the various relevant modulation frequencies). 0.6 Hz is a subharmonic of the fundamental vibration frequency of the mechanical cryocooler, allowing sequential microphonic reponses to vibration to be differenced while the wave plate passes Stokes parameters Q and $-Q$. Alternatively, since the wave plate rotation rate is controllable, we can choose to set the signal frequency at an irrational submultiple of the fundamental vibration frequency.

The dark bolometers and two thermistors used to monitor the temperature of the bolometer stage are also sampled at ~ 20 Hz. Basic cryogenic and other housekeeping data are sampled at a lower data rate. The data will be stored locally on a ruggedized portable computer located on the telescope, then transferred via FTP to our data analysis computer nightly. A synopsis of the stored data and thermometry channels are included as Tables 2.4 and 3.1.

The experiment is designed to run autonomously for weeks at a time. It will be controlled by UNIX-based scheduling software installed on a PC in a shed near the telescope. Commands will be sent by the scheduler to either the telescope control computer (a VAX system) or to the portable computer. The portable computer runs Windows and LabVIEW. Upon receipt of commands from the scheduler, the

Parameter	Frequency
AC Detector Bias	200 Hz
Sample Rate	20 Hz
Bolometer Response	20 Hz
Signal Low-Pass Filter	6 Hz
Cryocooler Fundamental Harmonic	2.4 Hz
Signal Frequency $4f_{wp}$	0.6 Hz
Systematic Wave Plate Emission $2f_{wp}$	0.3 Hz
Wave Plate Rotation	0.15 Hz
Signal High-Pass Filter	0.06 Hz

Table 2.3: Relevant Modulation Frequencies

Channel	Function	Coupling
L Diff	Light Bolometer Difference	DC
L +	Light Bolometer #1 Level	AC
L −	Light Bolometer #2 Level	AC
L Bias	Light Bolometers Bias Level	DC
D Diff	Diagnostic Bolometer Difference	DC
D +	Diagnostic Bolometer #1 Level	AC
D −	Diagnostic Bolometer #2 Level	AC
D Bias	Diagnostic Bolometers Bias Level	DC
TR1	Temperature Control Difference	DC
T1	Thermistor #1 Level	DC
TR2	Temperature Monitor Difference	DC
T2	Thermistor #2 Level	DC

Table 2.4: Data Channels

LabVIEW software will carry out such tasks as cycling the multistage sorption cooler for the bolometer stage, taking and storing data, and starting and stopping the wave plate rotation. The LabVIEW software will also return some data to the scheduler, so that the scheduler can automatically carry out tasks such as pointing, skydips, and calibration.

2.8 Integration of Receiver with Telescope

The Polatron receiver and supporting thermometry and signal readout equipment are housed in a rectangular metal equipment box (the "BBT") approximately 125 cm long and 75 cm on a side. The box is designed to be rolled along metal tracks into the telescope from the rear, when the telescope is stowed and pointing at the horizon (Figure 2.10). Alignment and support connections are made at the central aperture of the telescope, from which the BBT hangs. At the rear of the BBT is a breakout panel containing connections for the cryocooler helium lines, ethernet connections for the portable computer, AC power connections, BNC breakouts for specific signal and thermometry lines, and other auxiliary connections.

Figure 2.10: OVRO 5.5m telescope from rear in stowed position.

Chapter 3 Polatron Cryogenic System

In this chapter we discuss the two main elements of the Polatron cryogenic system: the 4.2 K mechanical cryocooler and the sub-Kelvin sorption cooler. After motivating the application of these technologies to this experiment, we discuss their detailed design and integration. A discussion of the microphonic and radio-frequency properties of the system then follows.

3.1 Introduction

All millimeter-wave instruments designed for measurement of cosmic microwave background signals use cooled detectors and radiation shields to lower the intrinsic background noise of the experiment. Due to the nature of the detectors involved, incoherent and coherent systems make use of radically different refrigeration techniques.

Incoherent-detector (for instance, bolometric) instruments measure the temperature increase of a thermally isolated detector exposed to broadband optical radiation. Due to the quantization of phonon energy propagating between the heat sink and the detector, bolometers typically require sub-Kelvin detector temperatures to approach photon noise limited performance and to bring the detector into the semiconducting regime. Sub-Kelvin temperatures are typically achieved through one of three methods: sorption pumping on liquid ^{3}He, adiabatic demagnetization of a paramagnetic salt, or dilution of ^{3}He through ^{4}He. In most observational applications, which require multi-hour hold times, these refrigeration techniques operate off a 1.4 K heat sink provided by a bath of pumped liquid ^{4}He, which is in turn buffered by a 77 K liquid N_2 bath. Cryogenic hold times are limited by the total power absorbed by a given stage and the heat of vaporization of the refrigerant. Although the sorption refrigerators are self-contained and recycle their relatively small quantities of cryogenic gas, the higher temperature baths boil off, with the gaseous product either lost to the atmosphere

or recollected for later condensation. Depending on the remoteness or complexity of the observing platform, refilling these baths can be an expensive, troublesome, and sometimes dangerous task, particularly during long campaigns. Furthermore, the use of liquid cryogens often sets limits on the orientation of instrument with respect to gravity.

Coherent-detector instruments such as POLAR and PIQUE (§1.4) amplify the electric field of CMB radiation directly. The noise intrinsic to such a measurement depends on the temperature of the amplifying transistor; once the field has been amplified, room-temperature electronics are adequate to analyze the signal. As a result, typical CMB instruments of this type require < 100 K operating temperatures. Such temperatures are easily achieved through use of commercial self-contained mechanical cryocoolers which use ^{4}He as a working fluid. Care must be taken in these experiments to limit the systematic effects due to vibration and electrical interference caused by the cryocooler motor.

The Polatron employs a closed-cycle cryogenic system to achieve bolometric operating temperatures of ~ 0.25 K. A synopsis of all cryogenic thermometry and heater channels is included as Table 3.1. A mechanical cryocooler provides intermediate-temperature heat sinks at 50 K and 4 K via refrigeration of a ^{4}He working fluid. A custom, multi-stage ^{4}He/^{3}He/^{3}He sorption cooler, which was invented for application to the Polatron, operates off the 4 K stage, achieving nearly 40 hours of hold time beneath 0.25 K. There are several advantages to this system: nonexpenditure of cryogenic liquids, gravity-independence in mechanical design, and autonomous operation. There are also several potential disadvantages: noise due to microphonic coupling of the bolometer signals to cryocooler vibration frequencies, radio-frequency interference generated by the cryocooler motor, and the reduced cooling power and limited lifetime and reliability of 4 K mechanical coolers.

3.2 Cooling Requirements

Bolometers must be in mechanical, electrical, and radiative contact with ambient temperature (300 K) materials. The limited cooling powers available at 0.25 K and 4 K require several layers of heat interception. The anticipated heat loads on each of these stages was calculated and minimized under the constraints that (i) the 4 K operating point be dedicated to sinking heat arising in operation of the multistage sorption cooler; and (ii) the 0.25 K operating point be dedicated to sinking power incident on the bolometers under severe loading conditions.

Thermal power input on each stage is calculated as follows.

- *Radiative power.* All components of the receiver can be approximated as radiating blackbodies of known emissivity ϵ, temperature T, and surface area A. The power emitted is described by the Stefan-Boltzmann relation

$$P_{rad} \sim \epsilon \sigma T^4 \times A, \tag{3.1}$$

where $\sigma \sim 6 \, \mathrm{pW/cm^2}/K^4$. Infrared radiative loads on a given temperature stage in the Polatron can be divided into three categories: emission from the high-area, low-emissivity vacuum vessel and radiation shields for higher temperature stages; emission from the environment transmitted by the vessel window and infrared blocking filters; and emission from the high-absorptivity (and hence high-emissivity) filters themselves. None of these contributions can be trivially neglected. In the Polatron, radiative power input is concentrated at the front end of the receiver, while cooling power is concentrated at the mechanical cryocooler in the rear. As a result, substantial thermal power is conducted along the radiation shields by copper braid.

- *Conductive power.* Conductive loads on a given temperature stage in the Polatron are dominated by wiring, typically small-diameter stainless or manganin, and mechanical supports, typically fabricated from G-10 or Vespel. These materials are selected for their low thermal conductivity. Conducted power is

described by

$$P_{cond} = \frac{A}{l} \times \int_{T_{low}}^{T_{high}} g(T)dT \tag{3.2}$$

where $g(T)$ is the thermal conductivity of the conducting material as a function of temperature, measured in W/K/cm; A is the cross sectional area of the conductor; and l is the length of material between two bodies at temperatures T_{high} and T_{low}. Although the number of science detectors in the Polatron is small, the large number of thermometry and diagnostic channels mean that the wiring conductivity is non-negligible, of order 100 mW at 4 K and 0.1 μW at 0.25 K. Longer wires reduce the conducted power, but increase the integrated capacitance and hence the susceptibility to pick-up. The mechanical supports are designed to conduct no more than the wires at any stage; this can be achieved with no loss in mechanical strength due to the cylindrical symmetry and orientation of the receiver with respect to gravity.

- *Applied heater power*, described by

$$P_{heat} = I^2 R \tag{3.3}$$

where I is the current applied to a wire or resistor of impedance R. As will be described, the multistage sorption cooler requires large (0.5 W) heat inputs into the 4 K stage during cycling. This is the dominant source of load on that stage.

As can be seen in Figures 2.1 and 3.4, the main locations of heat interception include the 50 K stage provided by the mechanical cryocooler, and a 0.5 K stage provided by the sorption intercooler. In the following sections, we discuss the two main components of the cryogenic system, and their integration.

Channel	Location	Component	Operating Power or Temperature
1	GM Stage 1	Diode Therm.	50 K
2	GM Stage 2	Diode Therm.	20 K
3	GM Stage 2	Heater	$0 - 30$ W
4	JT Stage	Diode Therm.	4 K
5	JT Stage	Heater	$0 - 1$ W
6	Cold Link	Diode Therm.	4 K
7	Cold Plate	Diode Therm.	5 K
8	IC ^{4}He Condensation Point	Diode Therm.	4 K
9	IC ^{4}He Pump	Diode Therm.	$4 - 50$ K
10	IC ^{4}He Pump	Heater	0.5 W
11	IC ^{4}He Pump Heatswitch	Diode Therm.	$4 - 50$ K
12	IC ^{4}He Pump Heatswitch	Heater	0.5 W
13	IC ^{3}He Pump	Diode Therm.	$4 - 50$ K
14	IC ^{3}He Pump	Heater	0.5 W
15	IC ^{3}He Pump Heatswitch	Diode Therm.	$4 - 50$ K
16	IC ^{3}He Pump Heatswitch	Heater	0.5 W
17	IC Still	GRT Therm.	$0.5 - 1.5$ K
18	IC Still	Heater	$0 - 10$ mW
19	UC Pump	Diode Therm.	$4 - 50$ K
20	UC Pump	Heater	0.5 W
21	UC Pump Heatswitch	Heater	0.5 W
22	UC Still	GRT Therm	0.25 K
23	Inner Radiation shield	Diode Therm.	4 K
24	Outer Radiation shield	Diode Therm.	50 K
25	Focal Plane	Diode Therm	4 K
26	JFET Stage	Diode Therm	120 K
27	JFET Stage	Heater	10 mW

Table 3.1: Thermometry Channels

3.3   Mechanical Cryocooler

The 4 K heat sink temperature required by the multistage sorption cooler is provided by a commercial cryocooler supplied by APD Cryogenics (Model HS-4; Figure 3.1). The cryocooler consists of three stages of refrigeration using [4]He working fluid: two Gifford-McMahon (GM) stages, which precool the fluid; and a Joule-Thomson (JT) expansion stage, which provides the base-temperature cooling. The cooler is designed to operate in any orientation, and provides a nominal 1 W of cooling power at 4.2 K. A thorough description of GM/JT coolers can be found in [2]. A synopsis of that description follows, with special emphasis on those topics which apply directly to the cryogenic performance of the Polatron.

The Gifford-McMahon stages precool room temperature [4]He beneath the inversion temperature necessary for Joule-Thomson expansion. A separate, electrically powered, water-cooled helium compressor provides a pressure differential P_{in}/P_{out}. Operation of rotary inlet and outlet valves in coordination with synchronous motion of the reciprocating displacer provides the refrigeration. The gas and displacer do no work on one another, since the pressure differential across the displacer is small and arises largely due to the cooling of the gas. Instead, the gas flows into the main volume or into a regenerator, depending on the status of the inlet and outlet valves and the position of the displacer. Two-stage GM coolers operate similarly, but allow for greater cooling power at a lower base temperature due to the improved pre-cooling of the gas. The low pressure differential across the displacer mean that the demands on the sliding displacer seal are low, increasing reliability.

In the case of the HS-4, the stroke length of the displacers has been custom-reduced to remove the slight impact the displacer would normally make on the end of the cylinder. Such a modification was intended to reduce vibration of the cooler, although no measurement of the vibration was made before the modifications took place.

The JT system cools [4]He gas by allowing an isenthalpic expansion of a high-pressure gas through a small nozzle. An ideal gas would experience no change in

Figure 3.1: Model HS-4 mechanical cryocooler from APD Cryogenics.

temperature under such an expansion. Non-ideal gases exhibit two molecular effects which produce opposite temperature changes upon JT expansion. The first is due to the increasing distance between gas molecules under expansion: the lower the pressure, the lower the potential energy of interaction and hence the lower the kinetic energy and temperature. The second is due to the incompressibility of the gas: at the high pressures in the nozzle stream, repulsive electrical forces between the gas molecules increase the kinetic energy and temperature. The inversion temperature beneath which the first term dominates depends on the atomic properties of the gas; for helium, that temperature is 40 K. Cryogenic JT stages therefore require a pre-cooling stage in which the gas temperature is brought beneath the inversion

GM displacers

Rotary valve

Regenerator

Regenerator

JT orifice

50 K

20 K

4.2 K

50' line
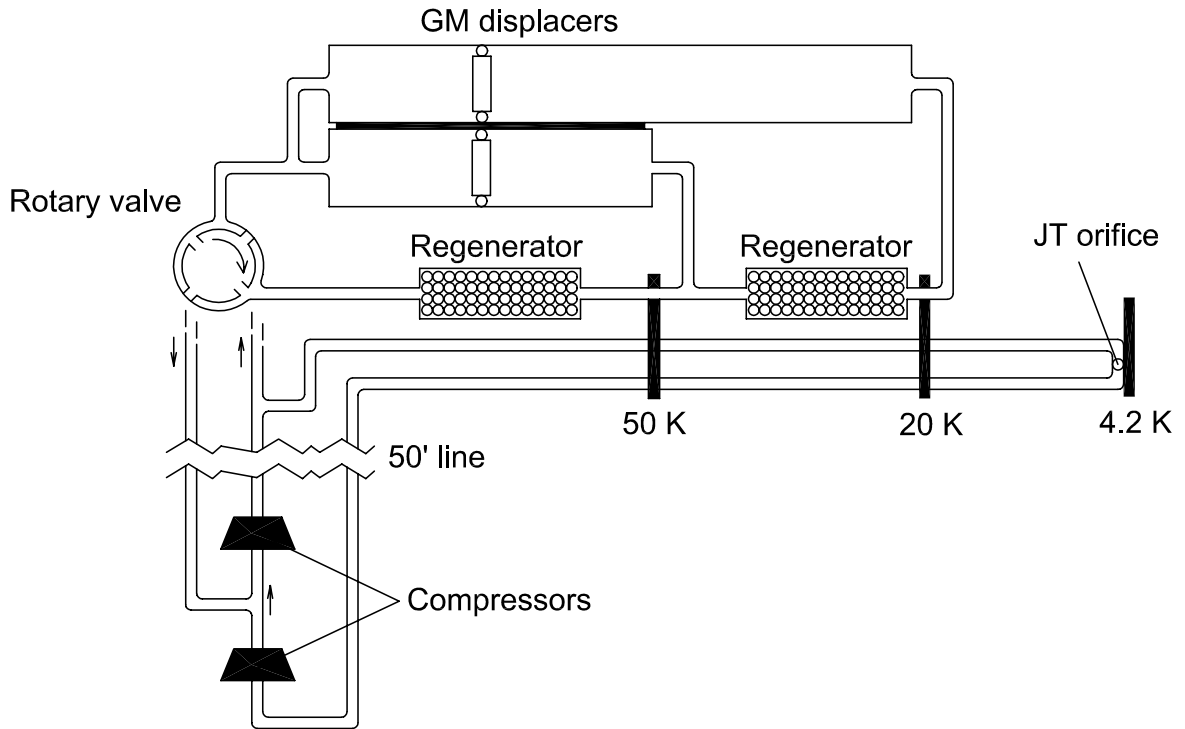
Compressors

Figure 3.2: Mechanical Cryocooler Schematic.

temperature so that expansion cools it further.

The HS-4 system integrates a two-stage GM cooler with a JT stage as shown in Figure 3.2. Two linked, oil-lubricated, water-cooled (18° C) helium compressors are required. These compressors consume several kW of power and will be installed on the azimuth platform of the telescope. Each is rated for 10,000 hours of performance before servicing. Four flexible helium lines 16 m in length run from the compressors to the cryocooler. The JT return line at the cryocooler contains cold gas beneath atmospheric pressure, so care must be taken to maintain the physical integrity of this line. The gravitational pressure drop due to the long length and position of the cryocooler above the compressors is negligible. A filter in the JT line prevents clogging of the expansion valve by impurities in the helium line, but requires servicing every 10,000 hours. Should such a clog occur, the system must be warmed to ambient temperature and re-cooled – no disassembly is required. The JT stage provides a stable 4 K heatsink; in contrast, 4 K GM coolers display instability in base temperature

which could generate systematic errors in our measurement [59].

The first GM stage provides a nominal 50 W of cooling power at 50 K. Radiation shields are heatsunk at this temperature to provide an intercept of optical and conductive loading from 300 K onto 4.2 K. The second GM stage provides a 20 K base temperature, but the cooling power at this stage is used entirely for pre-cooling of gas in the JT circuit. There is no provision in the system for heatsinking of radiation shields or thermally conductive wiring at this temperature. However, all components of the JT system are heatsunk at this temperature.

3.4   Multistage Sorption Cooler

Detector temperatures of 0.25 K are achieved with a custom, multi-stage ^{4}He/^{3}He/^{3}He sorption cooler that we designed in collaboration with Chase Research Cryogenics[1] for the Polatron. We begin with a review of the important properties of single-stage sorption refrigerators. A simple sorption refrigerator consists of two chambers: a pump chamber above a still, connected by a thermally isolating tube (Figure 3.3). The mid-point of the connecting tube – the "condensation point" – is attached to a cold, external bath. The pump is filled with an adsorbant material, such as charcoal, and is attached via a low thermal conductivity heat leak to the bath. The entire refrigerator is filled with a working fluid which is at a pressure of roughly 1 Atmosphere when the system is cooled to near the critical temperature T_{crit} of the fluid, above which temperature condensation cannot occur.

Sorption refrigerators are operated as follows: first, all elements of the refrigerator are cooled to well beneath T_{crit} through conduction between the working fluid and the condensation point. Then, heat is applied to the pump to raise its temperature above the adsorption temperature T_{ads} of the material in the pump for the given working fluid – this ensures that all gases have been expelled from the pump. As the working fluid liquifies at the condensation point, it drips down the connecting tube into the still. When most of the working fluid has been liquified, heat to the

---
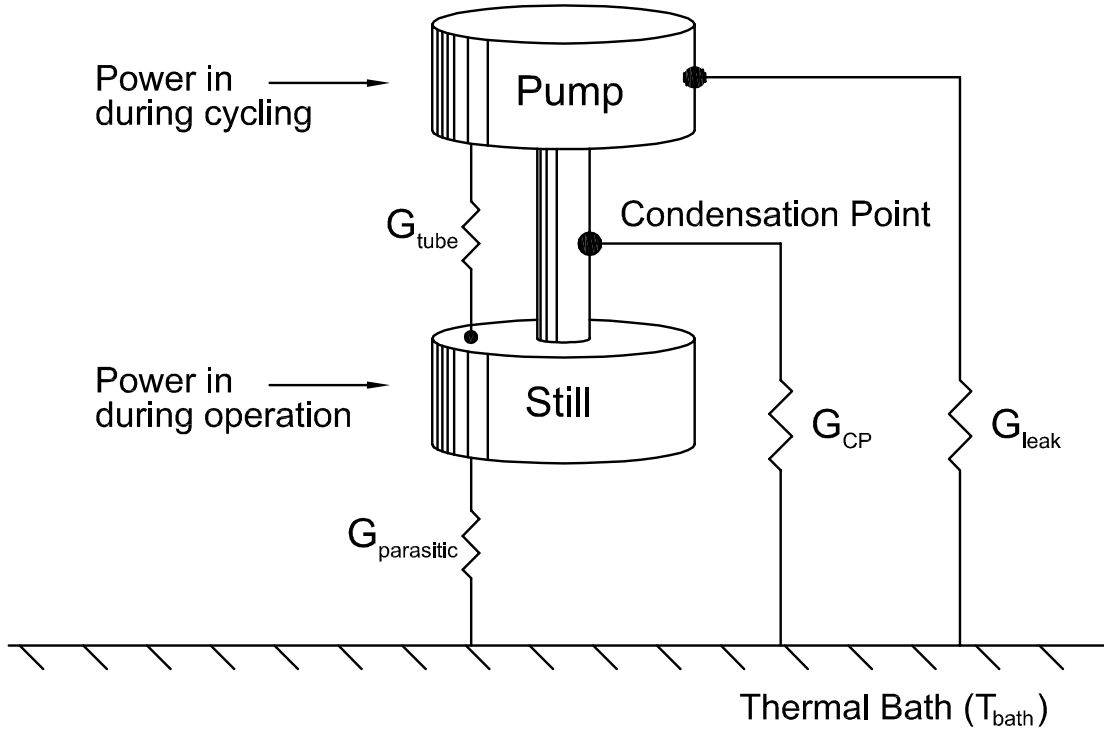
Figure 3.3: Schematic of a simplified sorption fridge.

Fluid	T_{crit}	T_{ads} (charcoal)	T_{base}	Q_{vap} @ 1.5 K
^{4}He	5.2	15 K	1.1 K	22 J/g
^{3}He	3.3	15 K	0.3 K	16 J/g

Table 3.2: Thermodynamic Properties of Helium[4]

pump is shut off, and it is allowed to cool. As the pump drops below T_{ads}, the vapor pressure of the liquid in the still drops, cooling the liquid. Greater heat input into the liquid raises both the base temperature T_{base} of the liquid and, to a greater extent, its vapor pressure. When the liquid is completely exhausted, the entire procedure can be repeated.

The critical temperature, charcoal adsorption temperature, pumped base temperature, and latent heat of vaporization of ^{4}He and ^{3}He are summarized in Table 3.2. A typical single-stage ^{3}He fridge operating off a large, pumped L^{4}He bath might provide 50 μW of cooling power at 0.3 K for 16 hours [20].

Figure 3.4 is a diagram of the thermal circuit of the Polatron multistage sorption cooler, separated into "intercooler" (IC) and "ultracooler" (UC) substages. An
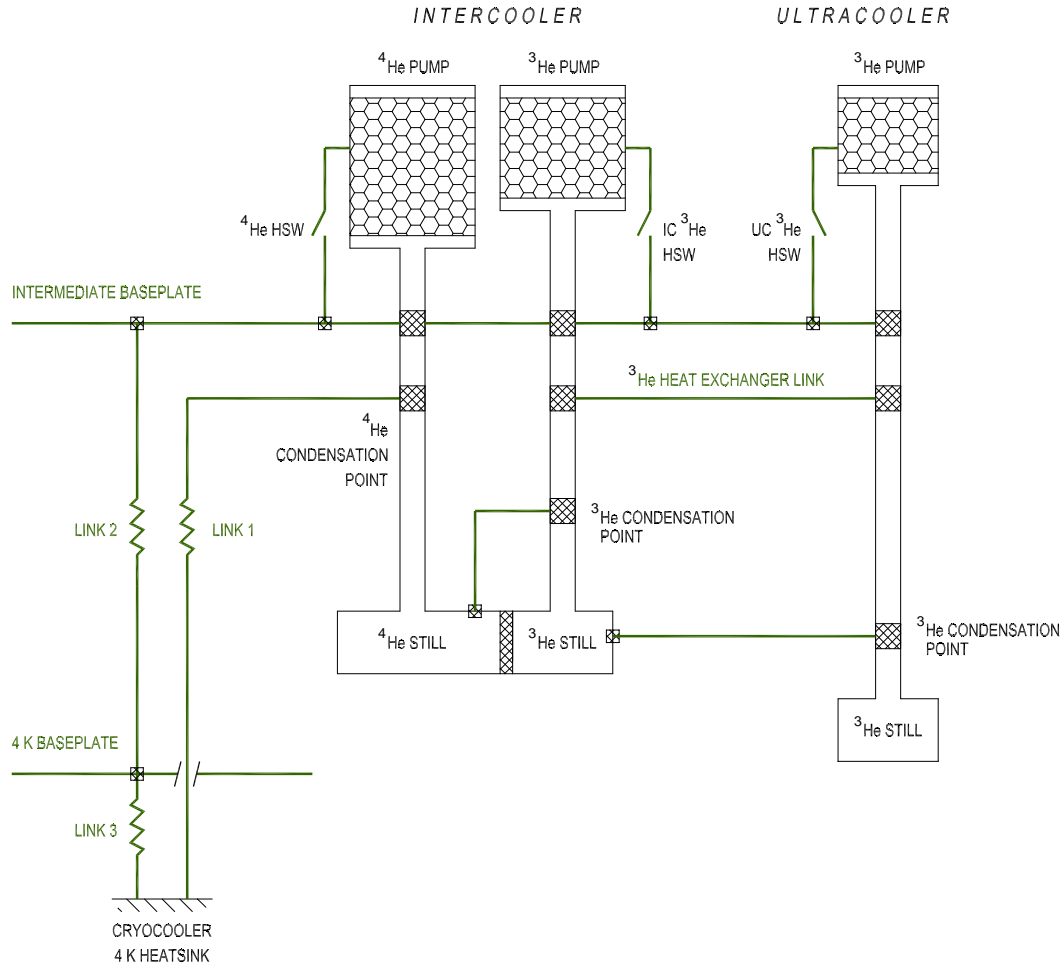
Figure 3.4: Diagram of the Thermal Circuit of the Polatron Multistage Sorption Cooler.

assembly schematic is included in Figure 3.5. The IC operates off a 4 K bath and, at two different times, provides intermediate temperature stages of 1.4 K and 0.5 K through the sequential operation of the IC ^{4}He and IC ^{3}He sorption coolers. The IC ^{4}He still is soldered directly to the IC ^{3}He still; however, the two fluids never intermix. The IC ^{4}He stage is cycled first. When the IC still temperature reaches 1.4 K, both the IC ^{3}He and UC ^{3}He stages are cycled. Condensation of ^{3}He in the IC and UC stages exhausts the ^{4}He liquid in the IC. The cooling power of the IC ^{3}He stage is used to intercept and reduce the heat load on the UC stage – as a result, the IC ^{3}He stage is heavily loaded.

The IC stage is designed to achieve a base temperature of 0.50 K for 12 hours
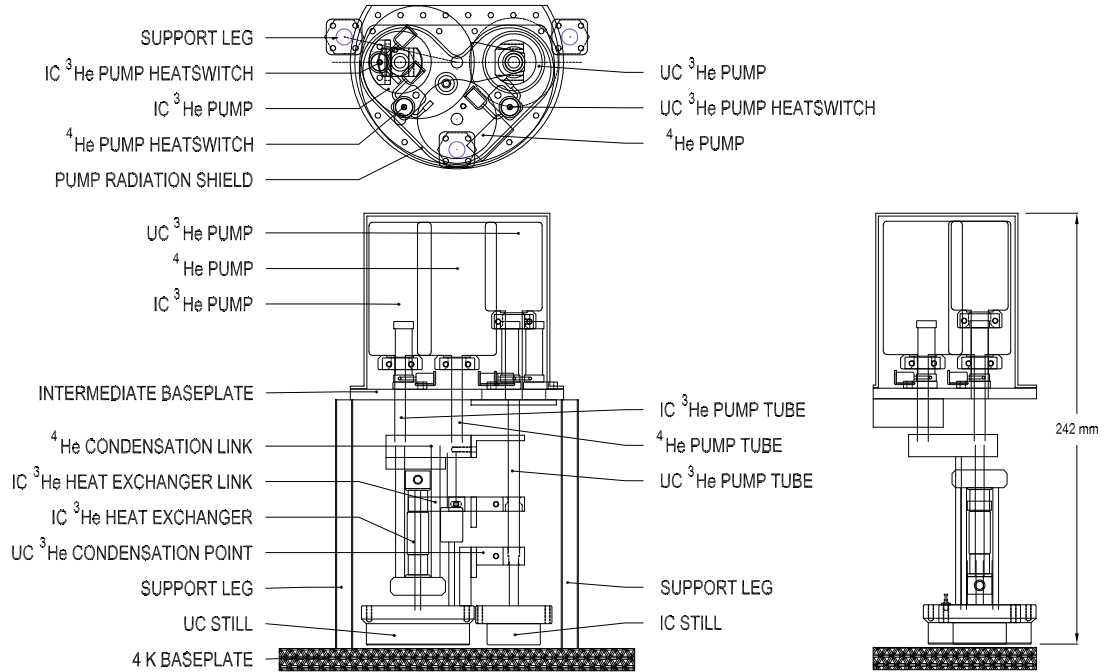
Figure 3.5: Assembly schematic of the Polatron Multistage Sorption Cooler, provided by Chase Research Cryogenics.

under a 115 μW load, while the UC stage is designed to achieve base temperatures of 0.25 K for the same time period, under a 3 μW heat load. Further design constraints included (*i*) a duty cycle > 80%; (*ii*) instantaneous power dissipation during cycling ΔQ < 0.5 W; and (*iii*) geometric constraints appropriate to the experiment.

3.5 Integration

Design of the interface between the mechanical cryocooler and the multistage sorption cooler is a deceptively straightforward engineering project. When the IC ^{4}He stage is cycled, the condensation point temperature rises by amount ΔT due to gas conduction of heat ΔQ from the pump. (Here we have assumed that all the heat of desorption of gas from the pump makes its way to the condensation point; this is a conservative assumption.) The mechanical cryocooler should sink this heat so that the condensation point temperature stays well beneath the critical temperature of ^{4}He. Hence, the condensation point of the IC ^{4}He stage and the cold tip of the cry-

ocooler must be thermally coupled with thermal conductivity G such that the power input ΔQ causes a temperature rise ΔT $<<$ T$_{crit}-$ T$_{bath}$.

As mentioned, the critical temperature of ^{4}He is 5.2 K, so we require ΔT $<$ 1 K. The power input during cycling a single refrigerator is $\approx$ 0.5 W. It follows that we require G $>$ 0.5 W/K. At 4.2 K, the thermal conductivity of OFHC Cu is 2.5 W/cm/K, so we require a length of OFHC copper with area to length ratio $A/l >$ 0.2 cm.

Ideally, the multistage sorption cooler would be integrated directly with the cryocooler, so that the cryocooler cold tip would be in direct contact with the IC ^{4}He condensation point. Milder constraints on the thermal conductivity between the UC still and the detectors (on the order of μW/mK rather than W/K) could allow the thermal link to be accomplished at sub-Kelvin temperatures. The Polatron cryogenic system was implemented with a LHe dewar-like cold plate off which the multistage sorption cooler and bolometer stage are suspended. Thus the thermal link is fairly complicated, as shown in Figure 3.4. A direct link runs between the cryocooler cold tip and the IC ^{4}He condensation point, while a separate, low-conductivity link runs from other 4 K elements (such as the feed structure) to a cold plate and then to the cryocooler tip. Furthermore, the heat of desorption of gas during each cooler cycle is dumped to the cold plate via the pump heat leak. In practice, the "4 K" cold plate runs at $\sim$ 5 K.

3.6 Microphonic and RFI Control

The mechanical cryocooler is a strong source of vibration. Microphonic vibration degrades signal quality through a variety of mechanisms: voltage noise generated by rapid changes in capacitance due to relative motion between signal and ground lines; induced voltage noise generated by motion of current loops through ambient magnetic fields; heating of the bolometer due to increased dissipated electrical power; varying optical signal due to motion and subsequent misalignment of optical elements; and an increase in bolometer sink temperature due to microphonic heating of the cold

stage. A review of these mechanisms, and how they degrade bolometric performance in particular, can be found in [4].

The most important step in mitigation of microphonic response is use of a low output-impedence JFET source-follower at each bolometer output (Figure 2.8). This limits the susceptible wiring to the high-impedance length between the bolometer and the JFET. This length is minimized under the constraint that the JFET and bolometer be sufficiently thermally isolated, as JFET noise performance is severely degraded beneath 110 K.

The Polatron employs a 10 cm length of twisted pair, shielded, stainless wire between the bolometer output and JFET input. The shields are tied to physical ground at the bolometer integrating cavity. Twisted-pair wiring mitigates microphonic capacitive and inductive coupling by forcing both wires to move in tandem. The JFET amplifiers are placed on circuit board which is suspended by G-10 supports from the 4 K cold plate. The temperature of the circuit board is raised to 120 K by power dissipation in the source resistors near the amplifiers. The suspension system has been stiffened to move the resonant frequency of the structure above the bolometric bias frequency, and the entire structure is placed in a 4 K Faraday cage. The bolometers themselves have reduced mass compared to typical composite bolometers due to their open-mesh geometry, and as such display reduced susceptibility to microphonic motion [4].

In order to mitigate systematic effects due to vibration-induced optical misalignment, the feed structure is laterally supported at the 4 K / 0.25 K thermal gap to maintain optical alignment.

Further mitigation of microphonic response is accomplished through the mechanical isolation of the cryocooler from the bolometer stage. This occurs in three locations: at the 300 K physical support of the cryocooler, at the 80 K stage, and at the 4 K thermal link between the cold plate and the cryocooler tip. The cryocooler is physically suspended from the vacuum vessel by stainless steel bellows supplied by National Electrostatics Corporation[2] (Figure 2.1). Atmospheric pressure forces the

---

[2]National Electrostatics Corporation, 7540 Graber Road, P.O. Box 620310, Middleton, WI 53562-
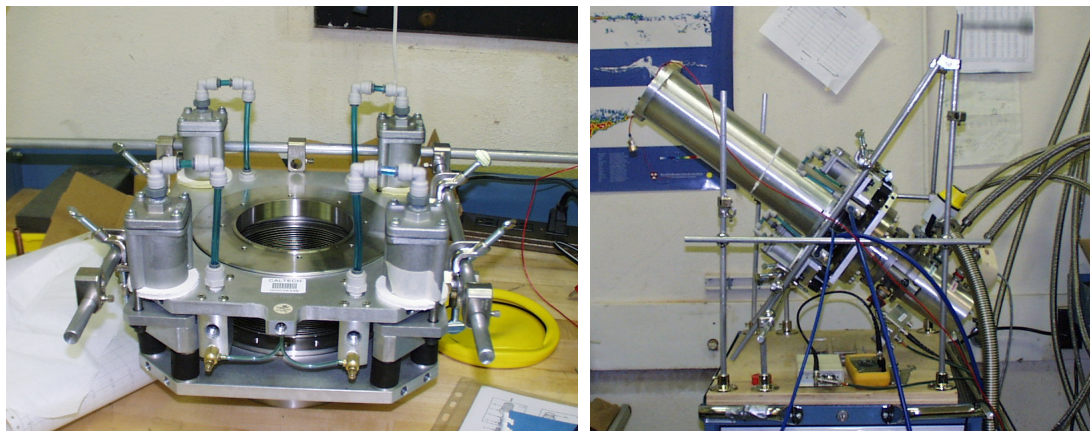
Figure 3.6: Left: pneumatic vibration isolator; Right: mechanical cryocooler operating at a 45° – vibration isolator is designed to comply with tilt in a single direction.

bellows closed while a leaked pneumatic air-suspension system provides a dissipative restoring force. The suspension system has two independent pressure levels allowing the system to retain mechanical isolation through a large range of tilt angles (Figure 3.6). Mechanical compliance at the 4 K thermal link is accomplished through a flexible coupling manufactured from OFHC Cu braid.

Vibrational energy can be dissipated in the 0.25 K bath, increasing the operating temperature and hence the noise level of the detectors. Each detector is directly attached to a copper ring which is bolted to the 0.25 K stage. By placing the two detectors in close thermal proximity, signal due to variations in heatsink temperature will be matched between the two detectors and rejected as common-mode signal.

The response to induced vibration of a silicon-nitride micromesh bolometric system with similar wiring and readout scheme was measured by Bhatia et al. [4]. The bolometers were operated at 0.3 and 0.1 K and subject to acceleration levels typical of vibration caused by space cryocoolers: $0 - 40$ mg between $0 - 25$ Hz. They conclude that standard mitigation techniques such as those described above adequately protected the system from microphonic systematics, with no noise above the quiescent NEP $\sim 2 \times 10^{-18}$W Hz$^{-1/2}$. It must be stressed that the variation in detector type, readout circuit, and mechanical design between experiments means that, although

these results encourage further examination of cryocooled bolometric systems, they do not in themselves guarantee successful operation.

Response to radio-frequency interference (RFI) is related to microphonic response in that the strongest source of RFI near the detectors is the cryocooler motor itself. Furthermore, electromagnetic fields generated in the cryocooler motor can increase inductive microphonic response. RFI couples to the high-impedance wires between the bolometer and the JFETs by driving currents, and can cause both voltage noise and bolometer heating.

Three design techniques were aimed at reducing RFI susceptibility of the Polatron: first, the bolometer stage is electrically isolated from the rest of the system via a Kapton thermal link between the multistage sorption cooler and the stage; second, as discussed, the 4 K stage acts as a Faraday cage with a single aperture at the feed horn throat; third, also discussed previously, all lines entering the 4 K space are RFI filtered [46].

Chapter 4 Observing Strategy

In this chapter, we introduce the basic observing strategy of the Polatron experiment. A calculation of the anticipated sensitivity follows, including a discussion of calibration methods. CMB polarization experiments are particularly susceptible to systematic effects, so we discuss the anticipated polarization systematics in this experiment and the anticipated confusion from polarized astrophysical foregrounds. The chapter ends with discussion of a proposed scan strategy.

4.1   Introduction

Before making a detailed calculation of instrumental sensitivity, it is useful to make an order-of-magnitude calculation of the sensitivity levels required to detect CMB polarization. Consider an idealized polarimeter with instantaneous sensitivity to Stokes parameter Q (or U) of 1 mK $\sqrt{s}$ which maps $N_p = 900$ pixels (1 square degree) in a ring about the north celestial pole with $\theta_b = 2'$ resolution for 6 months and 50% observing efficiency. Each pixel is observed to sensitivity $\sigma_T = 15~\mu$K in each of Q and U. The l-space window for such an experiment runs from approximately $l_{min} \sim (180°/1°)$ to $l_{max} \sim (180°/2')$, or $l \sim 180 - 5000$. Assuming that the measurement is not sample variance limited, the experiment is sensitive to *rms* polarization fluctuations at the level of 15 μK / $\sqrt{900}$ or $\sim 0.5~\mu$K in flat band power. Although the *rms* polarization level seen by such an experiment will vary with model, models which are compatible with the ΔT power spectrum measured by BOOMERANG predict roughly 2 – 4 μK of polarization power on these angular scales (see Figure 1.6). Therefore, our model polarimeter would either make a confident detection of polarization, or it would provide a challenging null result.

4.2 Anticipated Sensitivity

Five main sources of noise limit the ultimate sensitivity of the Polatron: photon noise, detector noise, amplifier noise, fluctuations in atmospheric emission, and non-atmospheric $1/f$ noise. We will estimate the contributions from the first four of these below. The quantitative results are summarized in Table 4.2. It is conventional to express the noise in terms of a Noise Equivalent Power (NEP), measured in units of W $\mathrm{Hz}^{-1/2}$. Experimental $1/f$ noise is difficult to predict in advance; mitigation of systematic errors due to $1/f$ noise is addressed by our scan strategy.

4.2.1 Photon Noise

Photon noise arises from quantum fluctuations in background emission from the atmosphere, telescope, and receiver environment. Calculation of the photon noise proceeds as follows. First, the emissivity and temperature of the loading environment are determined in order to calculate the thermal mode occupancy of the background photons. Then, the statistical variance in the mode occupancy is calculated. Finally, that variance is converted into a noise power. At times, calculation of the photon noise for the Polatron will proceed somewhat heuristically, preferring band-averaged quantities ($A \times \Delta\nu$) to differential spectral quantities ($A_\nu d\nu$). This is a reasonable approximation to make for a spectral bandwidth of $\sim 20\%$: the average discrepancy between predicted and actual sensitivity for an ensemble of CMB experiments is likely $>> 20\%$. This calculation is based on a more rigorous theoretical treatment of photon noise found in [63].

For the Polatron, the optical power is dominated by in- and out-of-band emission from the 118 GHz O_2 line, the strength of which remains fairly constant over changing weather conditions. The most variable component is the far wings of H_2O line emission at higher frequencies, which is quantified by the precipitable water vapor column density (*pwv*). Between September and May, *pwv* for the OVRO site typically ranges between 3 and 8 mm (see *www.ovro.caltech.edu* for a snapshot of the current and 30-day weather conditions). Measurements carried out by a dedicated radiometer of

the zenith atmospheric spectral transmission $t_z(\nu)$ at OVRO (see Figure 5.2) allow us to compute a band-averaged atmospheric emissivity

$$\epsilon = \int_0^\infty \eta(\nu)(1 - t_z(\nu))d\nu. \tag{4.1}$$

The atmospheric transmission will vary with thickness, and hence the altitude angle of a given observation. In the direction of the North Celestial Pole, we estimate $\epsilon = 0.2$ under 6 mm of *pwv*.

The average number of photons arriving at a single detector per second per Hz of spectral bandwidth per polarization state (#/s/Hz/pol) is given by Planck's expression

$$\bar{n} = \frac{\epsilon \, \eta_{opt}}{e^{h\nu/kT} - 1}, \tag{4.2}$$

where η_{opt} is the spectral efficiency of the optical chain between the detector and the source, not counting the polarization analysis. The variance in n, which is the source of photon noise, is given by

$$\langle (\Delta n)^2 \rangle \equiv \langle (n - \bar{n})^2 \rangle = \bar{n} + \bar{n}^2, \tag{4.3}$$

a consequence of boson counting statistics. The first term is interpreted as typical Gaussian statistics, while the second term can be interpreted as "bunching" in photon arrival time. For $\bar{n} \sim 1$, both the $\bar{n}$ and $\bar{n}$ terms are important. It is important to remember that this thermal mode number is separate from the number of spatial modes m in the beam decomposition, given by the throughput relation for radio telescopes $A\Omega = m\lambda^2$, where A is, to take one aperture, the illuminated area of the primary mirror, and Ω is the beam solid angle. As mentioned, for the Polatron, $m = 1$.

Assuming an atmospheric temperature of 280 K, emissivity $\epsilon \sim 0.2$, and optical efficiency $\eta_{opt} \sim 0.2$, we calculate

$$\bar{n} \sim 2.6 \times \left(\frac{\epsilon}{0.2}\right)\left(\frac{\eta_{opt}}{0.2}\right). \tag{4.4}$$

Thus, we cannot trivially neglect either term in the occupation variance.[1]

To calculate the optical power incident on a single detector, we weight $\bar{n}$ by energy $h\nu$ and integrate over the spectral band:

$$
\begin{aligned}
P_{opt} &= \int_0^\infty \bar{n} \times (h\nu) d\nu & (4.5) \\
&\sim \bar{n} \times (h\nu)\, \Delta\nu & (4.6) \\
&\sim 3 \text{ pW} \times \left(\frac{\bar{n}}{2.6}\right)\left(\frac{\Delta\nu/\nu}{0.2}\right) & (4.7)
\end{aligned}
$$

We now calculate the photon noise. Eqn. 4.6 can be rewritten

$$
\bar{n} \sim \frac{P_{opt}}{(h\nu)\Delta\nu}, \tag{4.8}
$$

so that Eqn. 4.3 for the variance now reads

$$
\langle(\Delta n)^2\rangle \sim \frac{P_{opt}}{(h\nu)\Delta\nu}(1+\bar{n}). \tag{4.9}
$$

The power variance in one second is the band-integrated mode-occupancy variance, weighted by photon energy:

$$
\begin{aligned}
\langle P_{opt}^2\rangle \times [1 \text{ sec}] &= \int_0^\infty \langle(\Delta n)^2\rangle(h\nu)^2 d\nu & (4.10) \\
&\sim \langle(\Delta n)^2\rangle(h\nu)^2\Delta\nu & (4.11) \\
&\sim P_{opt} \times (h\nu)(1+\bar{n}), & (4.12)
\end{aligned}
$$

where it has been assumed that upon integration over infinitesimal frequency bands $d\nu$ the contribution to the power variance is square-additive. The single detector photon $\text{NEP}_{ph,s}$ is the *rms* variance

$$
\text{NEP}_{ph,s} = \sqrt{2} \times \sqrt{P_{opt}\, h\nu\, (1+\bar{n})} \tag{4.13}
$$

---

[1]It has been argued, however, that the n^2 term has been neither fully justified nor experimentally measured in a bolometric system. Since its inclusion can be motivated by non-quantum considerations, it is argued the "bunching" term is integrated down over the bolometer response period $\tau \sim 25$ ms $\gg \nu^{-1}$. We include the term as a precaution against over-estimating our sensitivity.

$$\sim \quad 2.0 \times 10^{-17} \text{ W Hz}^{-\frac{1}{2}} \times (1 + \bar{n})^{1/2} \times \left(\frac{\bar{n}}{2.6}\right)^{\frac{1}{2}} \left(\frac{\Delta\nu/\nu}{0.2}\right)^{\frac{1}{2}} \quad (4.14)$$

$$\sim \quad 3.8 \times 10^{-17} \text{ W Hz}^{-\frac{1}{2}} \quad (4.15)$$

where the extra factor of $\sqrt{2}$ arises in the conversion from photons per second to Hz bandwidth.

An additional factor of $\sqrt{2}$ takes into account the fact that the noise in a measurement of Stokes parameter Q or U is the noise in the signal difference taken between two uncorrelated detectors:

$$\text{NEP}_{ph} \sim 5.4 \times 10^{-17} \text{ W Hz}^{-\frac{1}{2}} \quad (4.16)$$

4.2.2 Detector Noise

The second source of noise is fundamental thermal fluctuations in the detectors. Detector noise arises as phonon shot noise in the low conductivity (G) thermal link between the thermistor and the bath or as Johnson noise in the thermistor [63]. For our operating configuration at bolometer temperature T, the phonon noise is

$$\text{NEP}_{phon} \quad = \quad \sqrt{4k_B \text{T}_{bolo}^2 \text{G}} \quad (4.17)$$

$$\sim \quad 1.9 \times 10^{-17} \text{ W Hz}^{-\frac{1}{2}} \times \left(\frac{\text{T}_{bolo}}{0.43 \text{ K}}\right) \left(\frac{\text{G}}{80 \text{ pW/K}}\right)^{\frac{1}{2}} \quad (4.18)$$

where k_B is the Boltzmann constant. Note that the thermal conductivity G is itself temperature-dependent.

The expected Johnson noise

$$\text{NEP}_{john} \quad = \quad \frac{\sqrt{4k_B \text{T}_{bolo} \text{R}_{bolo}}}{\text{S}} \quad (4.19)$$

$$\sim \quad 2.3 \times 10^{-17} \text{ W Hz}^{-\frac{1}{2}} \times \left(\frac{\text{T}_{bolo}}{0.43 \text{ K}}\right)^{\frac{1}{2}} \left(\frac{\text{R}_{bolo}}{2 \text{ M}\Omega}\right)^{\frac{1}{2}} \left(\frac{3 \times 10^8 \frac{\text{V}}{\text{W}}}{\text{S}}\right) (4.20)$$

where S is an estimate of the electrical responsivity under the loading conditions

expected at the telescope (§5.5), and R$_{bolo}$ is a function of temperature (§2.4.7).

As above, the total differential detector noise is increased by $\sqrt{2}$ due to differencing:

$$\text{NEP}_{det} = \sqrt{2} \times \sqrt{\text{NEP}^2_{phon} + \text{NEP}^2_{john}} \tag{4.21}$$

$$\sim 2.9 \times 10^{-17} \text{ W Hz}^{-\frac{1}{2}} \tag{4.22}$$

4.2.3 Amplifier Noise

The third component of noise is amplifier noise in the cold matched JFETs. The measured differential noise performance of ~ 4 nV Hz$^{-1/2}$ is converted to estimated NEP by dividing by an estimate of the electrical responsivity S:

$$\text{NEP}_{amp} \sim 1.3 \times 10^{-17} \text{ W Hz}^{-\frac{1}{2}} \times \left(\frac{3 \times 10^8 \text{ V/W}}{S} \right) \tag{4.23}$$

4.2.4 Atmospheric Noise

The final component of noise is $1/f$ fluctuations in atmospheric water vapor content. Differencing the two detector signals rejects common-mode fluctuations. This technique is identical to that used in the Sunyaev-Zel'dovich Infrared Experiment (SuZIE), except that SuZIE differences the power in two spatial pixels, whereas the Polatron differences the power in two senses of linear polarization within the same spatial pixel. Since the atmosphere is not significantly polarized [38], atmospheric $1/f$ noise is limited only by the common mode rejection ratio (CMRR) of the receiver. Ground-based measurements of CMB polarization would not be feasible without cancellation of atmospheric fluctuations in this manner.

The level of residual atmospheric emission fluctuations at our signal frequency can be estimated using the methods of Church [10]. Since SuZIE and the Polatron have similar beam sizes, the atmospheric fluctuations observed by SuZIE at 217 GHz from Mauna Kea are scaled to obtain an estimate of atmospheric fluctuations that will be seen by the Polatron at 100 GHz from OVRO. This scaling relies on the following

assumptions: that residual atmospheric noise is dominated by gain mismatches and not beam mismatches; that Zeeman splitting of O_2 lines by the Earth's magnetic field is negligible [38]; that the gains of the two polarization channels can be matched on a regular basis to 1%; that fluctuations are due to variations in water vapor content; and that the OVRO atmospheric emission fluctuations can be estimated by frequency scaling Mauna Kea emission fluctuations, as measured by SuZIE.

The difference in atmospheric opacities at the two sites is encoded in the ratio

$$R_1 = e^{-\frac{\tau_S}{\sin\theta_S}} / e^{-\frac{\tau_P}{\sin\theta_P}} \tag{4.24}$$

$$\approx 2.0 \tag{4.25}$$

where typical measured 225 GHz zenith opacities $\tau_S = 0.07$ at Mauna Kea and $\tau_P \sim 0.5$ at OVRO, and the assumed altitude angles are $\theta_S \sim 60°$ and $\theta_P \sim 40°$. A second ratio, $R_2 = 0.18$, is a scaling factor which takes into account the difference in the contribution to the total atmospheric opacity due to water vapor at $\nu_P = 98$ GHz and $\nu_S = 217$ GHz (see Danese et al. [15]).

Following Church [10], we calculate

$$NEP_{atm} = \frac{1}{2}\frac{NEP_S}{CMRR} \times R_1 R_2 \times \left(\frac{A\Omega_P}{A\Omega_S}\right)\left(\frac{\nu_P}{\nu_S}\right)^2\left(\frac{(\Delta\nu/\nu)_P}{(\Delta\nu/\nu)_S}\right)\left(\frac{\eta_P}{\eta_S}\right). \tag{4.26}$$

The subscript P refers to the Polatron and S refers to SuZIE. The quantity $NEP_S = 1.0 \times 10^{-15}$ W Hz$^{-1/2}$ was measured by SuZIE at Mauna Kea in a single channel at the Polatron signal frequency $4f_{wp} = 0.6$ Hz. A factor of 1/2 is included to convert the SuZIE data to a single polarization. The dependence on spectral frequency and bandwidth arise in the thermal nature of the emission. A side-by-side comparison of the quantities relevant to a calculation of atmospheric fluctuations at the two sites can be found in Table 4.1. The anticipated noise can be rewritten

$$NEP_{atm} \sim 3.6 \times 10^{-19} \text{ W Hz}^{-\frac{1}{2}} \times \left(\frac{\Delta\nu/\nu}{0.2}\right)\left(\frac{\eta_{opt}}{0.2}\right). \tag{4.27}$$

Quantity	SuZIE	Polatron
CMRR	1	100
Altitude Angle θ	60	40
Zenith Opacity τ (@ 225 GHz)	0.07	0.5
Observing Opacity $e^{-\tau/\sin\theta}$	0.92	0.46
Throughput $A\Omega$ (mm^2)	13.0	9.8
Frequency ν (GHz)	217	96
Bandwidth $\Delta\nu/\nu$	0.07	0.2
Optical Efficiency η_{opt}	0.4	0.2
# of Polarizations	2	1

Table 4.1: Comparison of quantities used to calculate expected atmospheric fluctuations for SuZIE and Polatron

4.2.5 Flux Sensitivity

The total differential noise performance of the system is predicted by adding the NEP from each source in quadrature:

$$\text{NEP}^2_{total} = \text{NEP}^2_{ph} + \text{NEP}^2_{det} + \text{NEP}^2_{amp} + \text{NEP}^2_{atm}. \tag{4.28}$$

The NEP is converted to Noise Equivalent Polarized CMB Temperature, NEPT_{cmb}, measured in $\mu\text{K}s^{1/2}$, as follows. First, we calculate the Noise Equivalent Polarized Flux Density (NEPFD), measured in Jy s$^{1/2}$, which is the sensitivity of the receiver to polarized light in a single second of integration time:

$$\text{NEPFD} \sim \frac{\text{NEP}_{total}}{\Delta\nu \times \eta_{opt} \times \text{A} \times \sqrt{2}} \tag{4.29}$$

$$\sim 10.8 \text{ mJy s}^{1/2} \times \frac{\text{NEP}_{total}}{[10^{-17} \text{ W Hz}^{-1/2}]} \times \left(\frac{0.2}{\Delta\nu/\nu}\right)\left(\frac{0.2}{\eta_{opt}}\right) \tag{4.30}$$

where A ~ 16.3 m^2 is the illuminated area of the telescope primary, and the factor of $\sqrt{2}$ arises in the conversion from Hz$^{-1/2}$ to s$^{1/2}$: the bandwidth of a "boxcar" filter on data sampled for time τ is $1/2\tau$. The total CMB flux density in both polarizations, F$_{cmb}$, measured in Jy, is

$$\text{F}_{cmb} \sim \frac{2h\nu \times \bar{n}}{\lambda^2} \times \Omega \tag{4.31}$$

pwv (mm)	NEP_{ph}	NEP_{bolo}	NEP_{amp}	NEP_{atm}	NEP_{tot}	NEPFD (mJy $\sqrt{s}$)	NEPT ($\mu K \sqrt{s}$)
3	4.9	2.9	1.3	.03	5.8	62	435
6	5.4	2.9	1.3	.04	6.2	67	470
8	5.9	2.9	1.3	.05	6.7	73	512

Table 4.2: Anticipated Sensitivity. Differential NEPs are given in units of $10^{-17}\,\mathrm{W\,Hz^{-1/2}}$.

$$\sim\quad 184.8\ \mathrm{Jy}, \tag{4.32}$$

Here $\Omega \sim 6 \times 10^{-7}$ sr is the beam solid angle, and $\bar{n} \sim 0.2$ has been evaluated for T_{cmb} = 2.7 K. Converting from intensity to CMB polarization temperature, the NEPT_{cmb} is then

$$\frac{\mathrm{NEPT}_{cmb}}{\mathrm{T}_{cmb}} = \frac{e^x - 1}{xe^x} \times \frac{\mathrm{NEPFD}}{\mathrm{F}_{cmb}}, \tag{4.33}$$

where $x = h\nu/k\mathrm{T}_{cmb} \sim 1.7$. Here, the NEPT is referring to the sensitivity to Stokes parameter Q (μK) in a second of observing time. Calculated NEPFD and NEPT_{cmb} for different atmospheric conditions are included in Table 4.2.

Quoting anticipated or realized sensitivities for CMB polarization experiments is made difficult by the various factors of 2 which may enter calculations. One convenient method for testing what one means by a polarization NET (or NEPT) is to consider the case that the two components of linear polarization are summed rather than differenced, in which case a conventional CMB ΔT measurement would result. Omitting the (much) increased noise arising in common-mode atmospheric fluctuations, the equivalent experimental NET should be the listed NEPT. Such an experiment, of course, loses a factor of $\sqrt{2}$ in sensitivity by splitting the polarization and then adding the two uncorrelated detectors.

4.3 Calibration

Calibration of the absolute responsivity of the instrument will be accomplished through single-polarization observation of largely unpolarized sources, such as planets. Each single-channel signal will be dominated by the atmospheric fluctuations described

above. As before, the level of such fluctuations observed with the SuZIE receiver can be scaled to predict noise levels for the Polatron, albeit with no common-mode rejection and no advantage due to the polarization modulation at $4f_{wp}$. A typical drift scan over a calibrator occurs over a time period of ~ 30 seconds. We expect a single-channel NEFD on those time scales of ~ 70 Jy $\sqrt{s}$. The anticipated flux from a typical calibrator (Mars, for instance) is on the order of several hundred Jy, so several drifts over the same source may be required in poor weather. Hence, calibration uncertainty will be dominated, as it is in the SuZIE experiment, by the uncertainty in the brightness of the calibrators themselves. We expect to flux calibrate to the 5-10% accuracy typically achieved for CMB observations.

4.4 Systematic Polarization

Until recently, millimeter-wave polarimetry has consisted mainly of the study of magnetic fields through the measurement of the polarization patterns of molecular clouds and compact dusty sources. The quantity of scientific interest for these studies has been the *degree of polarization* (or, simply, *polarization*) of a source, a vector-like quantity which has an alignment direction θ_{source}, modulo rotation by 180°, and positive fractional magnitude $0 < p_{source} < 1$ for every observed position (θ, ϕ) on the sky. This quantity is often denoted $\bar{p}_{source}(\theta, \phi)$; maps of this pseudo-vector field are often overlaid on emission intensity contours so that the relationship between the magnetic field and the emissive structure of the source is demonstrated.

Typical dust sources are polarized at the $1 - 10\%$ level, so a clean measurement of such should be accurate to $< 1\%$. A useful quantity to define is the fractional *systematic polarization*, $\bar{p}_{sys}$, of a system, which is the percentage polarization measured when an intrinsically unpolarized source is observed. By definition this quantity does not vary with source brightness. It is usually caused by, and fixed with respect to, the telescope and receiver. One can determine the extent of systematic polarization by measuring the observed polarization from source which is known to be unpolarized. It can also be measured through observation of a known polarized source over

a period of time such that the parallactic angle of the source rotates with respect to the telescope. The polarization as a function of time measured in the telescope's coordinate frame should describe a circle with radius p_{source} and center offset by $\bar{p}_{sys}$ from the origin. Once $\bar{p}_{sys}$ is measured in this way it can be simply subtracted pixel by pixel from maps of observed polarization $\bar{p}_{obs}(\theta, \phi)$:

$$\bar{p}_{source}(\theta, \phi) = \bar{p}_{obs}(\theta, \phi) - \bar{p}_{sys}. \tag{4.34}$$

In the low signal-to-noise regime, polarization percentage can be a difficult quantity to analyze, since it is not Gaussian-distributed about a mean of zero. To remedy this, reduced (fractional) Stokes parameters $q = Q/I$ and $u = U/I$ are introduced, with Q and U the measured Stokes parameters and I the measured source intensity. The quantities q and u can be positive or negative. The systematic polarization adds in the same way as before:

$$q_{source}(\theta, \phi) = q_{obs}(\theta, \phi) - q_{sys}, \tag{4.35}$$

$$u_{source}(\theta, \phi) = u_{obs}(\theta, \phi) - u_{sys}. \tag{4.36}$$

The polarization pattern can still be recovered since $p_{source} = \sqrt{q_{source}^2 + u_{source}^2}$ and $\theta_{source} = \frac{1}{2}\tan^{-1}(U/Q)$.

For measurements of bright, polarized sources such as dust and molecular clouds, this characterization of systematic errors relating to polarization is adequate. CMB polarization measurements, however, are different. It is the non-normalized Stokes parameters Q and U that are of interest, not the fractional polarization p or the reduced parameters q and u. The underlying intensity distribution is bright, with temperature 2.728 K, and extremely uniform, but varying across the sky with some likely unknown amplitude $\Delta T/T > 10^{-5}$. Hence, given a measurement of systematic polarization q_{sys} from observation of an unpolarized source, the resultant systematic $Q_{sys}(\theta, \phi) = q_{sys}T(\theta, \phi)$ cannot be simply calculated and subtracted from the data, since $T(\theta, \phi)$ is, as yet, unknown. Since we are looking for fluctuations $\Delta Q/T \sim 10^{-6}$,

we require q_{sys} and $u_{sys} \leq 0.01$ to ensure that we are not systematically polarizing ΔT fluctuations. An observing strategy which measures the polarization of a single pixel at different parallactic angles allows this systematic polarization to be subtracted to $< 1\%$ even if the underlying intensity distribution is unknown.

Signal pick-up in the far sidelobes of the main beam can affect faint-background measurements if the source in the sidelobes is bright enough. The sun, the moon, the galaxy, and the horizon are examples of such sources. In addition, for polarization measurements, the two components of linear polarization will have different beam shapes, since the polarization analyzer (in our case the OMT) defines a set of coordinates with respect to the receiver, telescope, and telescope surroundings. The differential pick-up from the source in the two beams should not be greater than the expected CMB polarization signal. The observation strategy, then, is subject to a certain set of restrictions on the angle between the observed region of sky and these various sources. Observation near the North Celestial Pole mitigates all of these effects.

4.4.1   Systematic Polarized Flux

In contrast to the systematic polarization described above, which amounts to a *percentage* polarization acquired by an observed unpolarized source, the Polatron will observe a variety of systematic polarized fluxes which are independent of the brightness of an observed source. For instance, thermal radiation from the surrounding environment will scatter from the telescope feed legs into our system, picking up some polarization during the scattering. This type and most types of polarized flux will vary slowly, and will be removed from the data as a DC-level while drift-scanning. While actively scanning the telescope, spurious signals can be removed by referencing them to the telescope's surrounding environment, while astrophysical sources will rotate about the North Celestial Pole.

The wave plate itself is a source of systematic polarized flux. As a consequence of the method used to produce birefringence, the two crystal axes of the wave plate incur

differing loss tangents and reflectivities. Unpolarized sky radiation incident on the plate will be converted to a systematic flux. This signal, however, will be modulated at $2f_{wp}$ and will not contribute to the signal after lock-in at $4f_{wp}$.

4.4.2 Receiver Polarization

Gain mismatches between the two bolometer channels generate a fractional systematic polarization such that an unpolarized source of intensity $I(t)$ incident on the receiver will produce a signal $Q'_{rec}(t) = q'_{rec}I(t)$ which is *not* modulated by the wave plate at frequency $4f_{wp}$. The magnitude of the receiver polarization is inversely related to the common mode rejection ratio of the instrument: $|q'_{rec}(t)| = 1/CMRR$. If the input intensity $I(t)$ varies on time scales $t \sim 1/4f_{wp}$, then the demodulated signal at $4f_{wp}$ will include components of $I(t)$. An example of this effect was treated earlier (§2.5) for the case of unpolarized sky fluctuations. As discussed in §4.2.4, we expect CMRR performance for the Polatron at or above a factor of 100 due to bias trim of the individual detector responsivities. In other words, the receiver polarization can be reduced to beneath 1% by adjustment of the relative gains of the two polarization channels.

Another source of common-mode signal is variation in the temperature of the bolometer stage. Variations at frequency $4f_{wp}$ will be recorded as signal. Because the gain differs for optical signals incident on the receiver as opposed to thermal signals at the bolometers themselves, a specific relative gain adjustment which trims out common-mode optical signals is not likely to also trim out common-mode temperature fluctuations. For this reason the bolometer stage will be temperature controlled to ~ 100 nK Hz$^{-1/2}$ stability using methods described in Holzapfel et al. [29].

4.5 Astrophysical Foregrounds

The Polatron spectral band is close to the minimum of contamination estimated to arise from observing through our own galaxy. Polarized foreground processes

include synchrotron emission, free-free emission, thermal dust emission, and, perhaps, emission from spinning dust grains.

Galactic synchrotron emission is likely to be highly polarized. Bouchet et al. [6] point out that spectral index and polarization information obtained from long-wavelength observations of galactic synchrotron might not extend to millimeter wavelengths. Nevertheless, by making the assumptions that the emission is 44% polarized and has the same spatial distribution as the unpolarized emission at long wavelengths, they predict at 100 GHz the following angular power spectra between galactic latitudes 30° and 75°:

$$C_G^{synch} = 0.9 \, l^{-3} \, \mu K^2 \tag{4.37}$$

$$C_C^{synch} = 0.9 \, l^{-3} \, \mu K^2. \tag{4.38}$$

Observations of galactic dust regions at 100 μm indicate that where dust emission is bright, the level of polarization is of order 2% [26] apart from a few small regions in which the polarization rises to 10%. However, the degree of polarization of high latitude cirrus emission is unknown. A model for high-latitude galactic dust polarized emission has been created by Prunet et al. [61]. This model assumes that cirrus is traced by observed H I emission and that the dust grains are similar in shape to those observed by Hildebrand et al. [26]. A 17.5 K Planck spectrum with emissivity proportional to ν^2 is assumed. The dust grains are expected to align with the galactic magnetic field; in order to make a conservative estimate, an unfavorable orientation for the magnetic field is used. The assumed intrinsic dust polarized emissivity of $\sim 30\%$ is reduced due to projection effects. At 100 GHz, the angular power spectra predicted by Bouchet et al. between galactic latitudes 30° and 75° are

$$C_G^{dust} = 8.9 \times 10^{-4} \, l^{-1.3} \, \mu K^2 \tag{4.39}$$

$$C_C^{dust} = 10.0 \times 10^{-4} \, l^{-1.4} \, \mu K^2. \tag{4.40}$$

Free-free emission in H II regions, like the CMB, can pick up some small polar-

ization through Thomson scattering. This is likely to generate a level of polarization much lower than that of synchrotron radiation. Likewise, the spinning dust grains proposed by Draine et al. [19] should not be polarized at or near the level of synchrotron emission. Neither of these is likely to contaminate our measurements. The galactic synchrotron and dust polarized emission at 100 GHz is thus estimated to be more than an order of magnitude below the CMB signal over the l-range to which the Polatron is sensitive (see Figure 4.1).
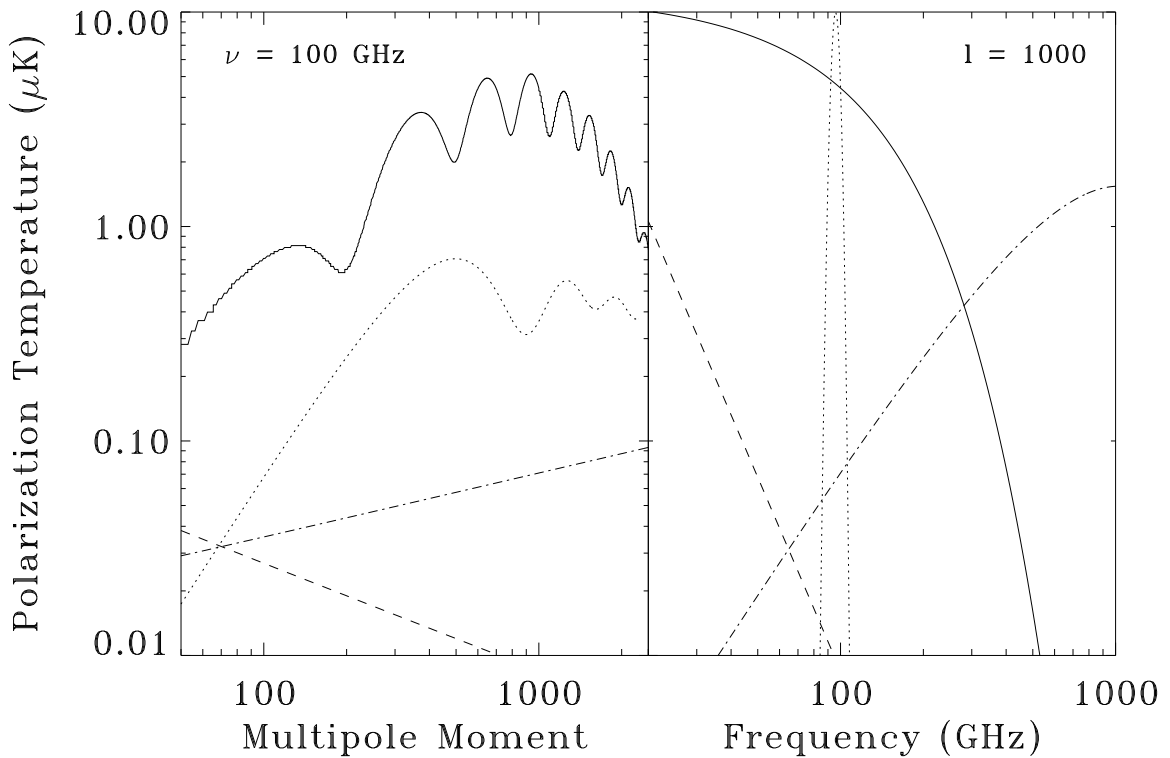

Figure 4.1: Polarization Galactic Foreground Spectra. Left panel: predicted polarization flat band power at 100 GHz as a function of multipole moment l for model CMB G-type fluctuations (solid line), galactic synchrotron (dashed line), and galactic dust (dash-dotted line). The dotted line indicates a generic Polatron window function in arbitrary units (see §4.6.) Right panel: predicted polarization flat band power at $l = 1000$ as a function of spectral frequency, same linetype key, with dotted line indicating the chosen Polatron spectral passband in arbitrary units. Temperatures are stated in Rayleigh-Jeans units. CMB G-type angular spectrum was generated by CMBFAST [12] for a BOOMERANG-consistent CDM universe.

4.6 Scan Strategy

Independent measurements of Stokes parameters Q and U at several separate locations on the sky are necessary in order to determine the polarization multipole moments described in Eqn. 1.21. If too few independent measurements are made, then the sample size is too small to determine an accurate variance in the Stokes parameters. If too many independent measurements are made, then each measurement will suffer from noise due to short integration time. The sample size is fundamentally limited by the number of independent measurements one can make on the sphere.

Design of an optimum scan strategy is not only influenced by sample size considerations. Environmental and scientific considerations also play a role. Several environmental considerations led us to consider observations of regions near the north celestial pole (NCP): when observing near the NCP, diurnal motion requires only slight motion of the telescope with respect to its physical environment, reducing sidelobe modulation; the NCP is $> 67°$ north of the ecliptic plane in summer, so the Sun, Moon, and planets are located well behind the telescope; furthermore, enough CMB experiments have observed near the NCP that there is more – but still scant – knowledge about galactic foregrounds in that region [44].

Initially, the scientific goal of the experiment will be to detect significant rms polarization on all angular scales to which the experiment is sensitive. This amounts to generating a broad window in l-space and observing fewer pixels, so that the noise per pixel is lower. After a detection has been made, and it is clear that the detection is not limited by systematic effects, the Polatron beam size is well-suited for spatial spectroscopy of CMB polarization. A greater number of pixels will be observed in a given amount of time, and the data will be binned in multiple l-space windows in order to search for acoustic peaks.

Since CMB temperature anisotropy generates polarization, one could use a measured ΔT map to locate regions with large temperature gradients. Observations intended to detect polarization signal might focus on these regions. In the absence of high-resolution, high signal-to-noise ΔT maps, however, a scan strategy can be

designed which takes advantage of the statistical relationship between temperature and polarization power spectra.

In the presence of $1/f$ noise, simple drift scan measurements on rings about the NCP are degraded by long time-scale correlations. The Ring 5m/40m experiment, which used the OVRO 5.5m telescope to measure ΔT fluctuations in NCP rings, held the telescope at a fixed elevation and performed regular 6h nods in right ascension [44], differencing the measured values to remove long-timescale drifts.

In Philhour et al. [58], the sensitivity of the Polatron to CMB polarization is estimated as a function of ring opening angle θ_{ring}. Inputs to the sensitivity model include the anticipated beam size, instantaneous sensitivity to Stokes parameters Q and U, and polarization power spectra C_l^G and C_l^C generated by CMBFAST [12] for a range of models consistent with the temperature power spectrum measured by BOOMERANG. Model window functions are generated with response peaked at the CMB polarization power spectrum peaks. Figure 4.2 plots detection signal-to-noise as a function of ring opening angle for three different total integration times. Results for a system without $1/f$ noise, with $1/f$ noise, and with $1/f$ noise and the nod strategy discussed above are included.
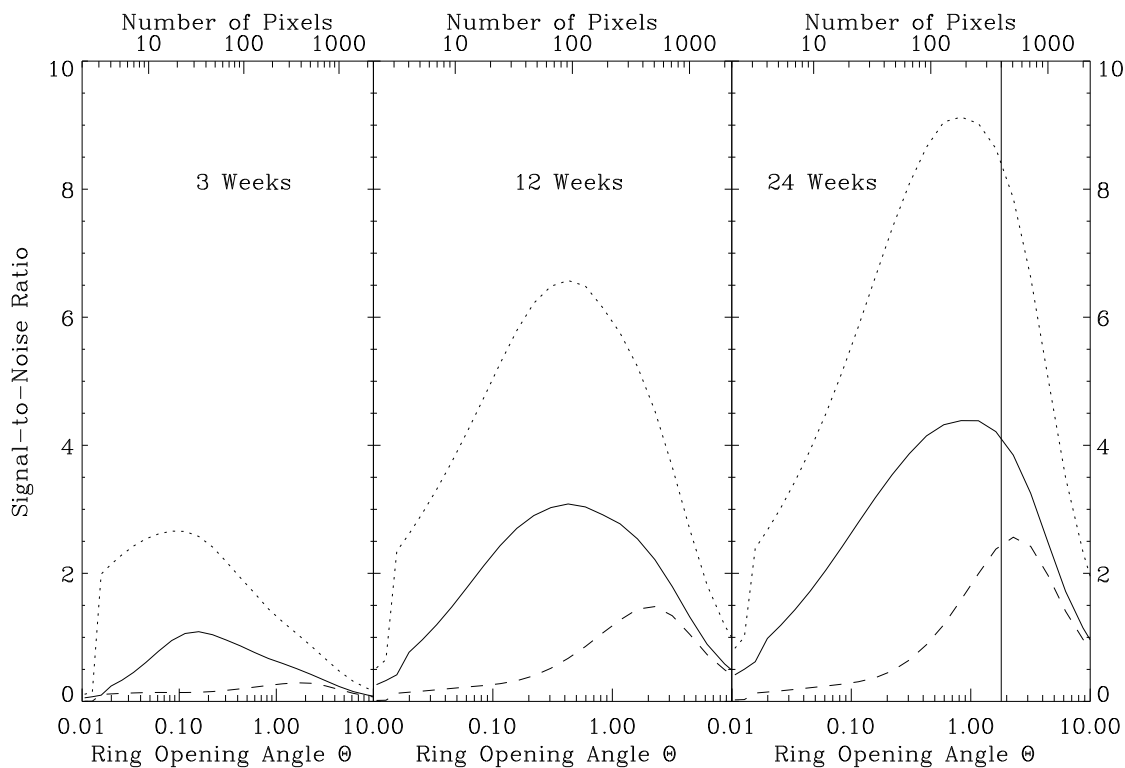
Figure 4.2: Polarization Sensitivity as a Function of Ring Opening Angle. Shown are three different total integration times for an instrument which measures both Stokes Parameters Q and U with the anticipated Polatron instantaneous sensitivity. Dotted curves represent anticipated signal-to-noise ratio under ideal instrument performance (no $1/f$ noise). Dashed curves represent the same measurement in the presence of $1/f$ noise. The solid curves represent performance in the presence of $1/f$ noise, but pairs of Q and U are differenced in pairs separated by 6h in Right Ascension about the NCP. Angular power spectra consistent with BOOMERANG measurements is assumed, as discussed in the text.

Chapter 5 Laboratory Characterization — Optics

Polarization analysis capability adds a new dimension to the optical characterization of millimeter-wave instruments. This chapter details the laboratory characterization of the Polatron optics in a separate optical testbed.

5.1 Introduction

In order to gain familiarity with the focal plane without the additional complication of the mechanical cryocooler and its associated hardware, we performed extensive testing on the Polatron focal plane in a separate optical testbed. An Infrared Labs[1] HDL-8 liquid He dewar outfitted with a Chase Laboratories ^{3}He sorption cooler provided a 0.30 K operating point for the bolometers (Figure 5.1). Measurements of the spectral pass-band, optical efficiency, polarization efficiency, sensitivity, and detector properties for the entire system, including the wave plate, were performed. The differential noise performance of the test receiver is adequate for optical testing purposes, but lacked the $1/f$ stability needed for CMB observations at the telescope. For this receiver, the bolometers were DC-biased, and no efforts were made to mitigate radio-frequency pickup or microphonic pickup. Furthermore, no trim circuit was available to balance the responsivities of the detectors, meaning the system was even more susceptible to fluctuations in the bolometer stage temperature and other low-frequency common mode signal.

5.2 Spectral Bands

Spectral bands $\eta(\nu)$ were measured independently for the two polarization channels using a Fourier Transform Spectrometer (FTS). The FTS consists of a 500 K / 77 K

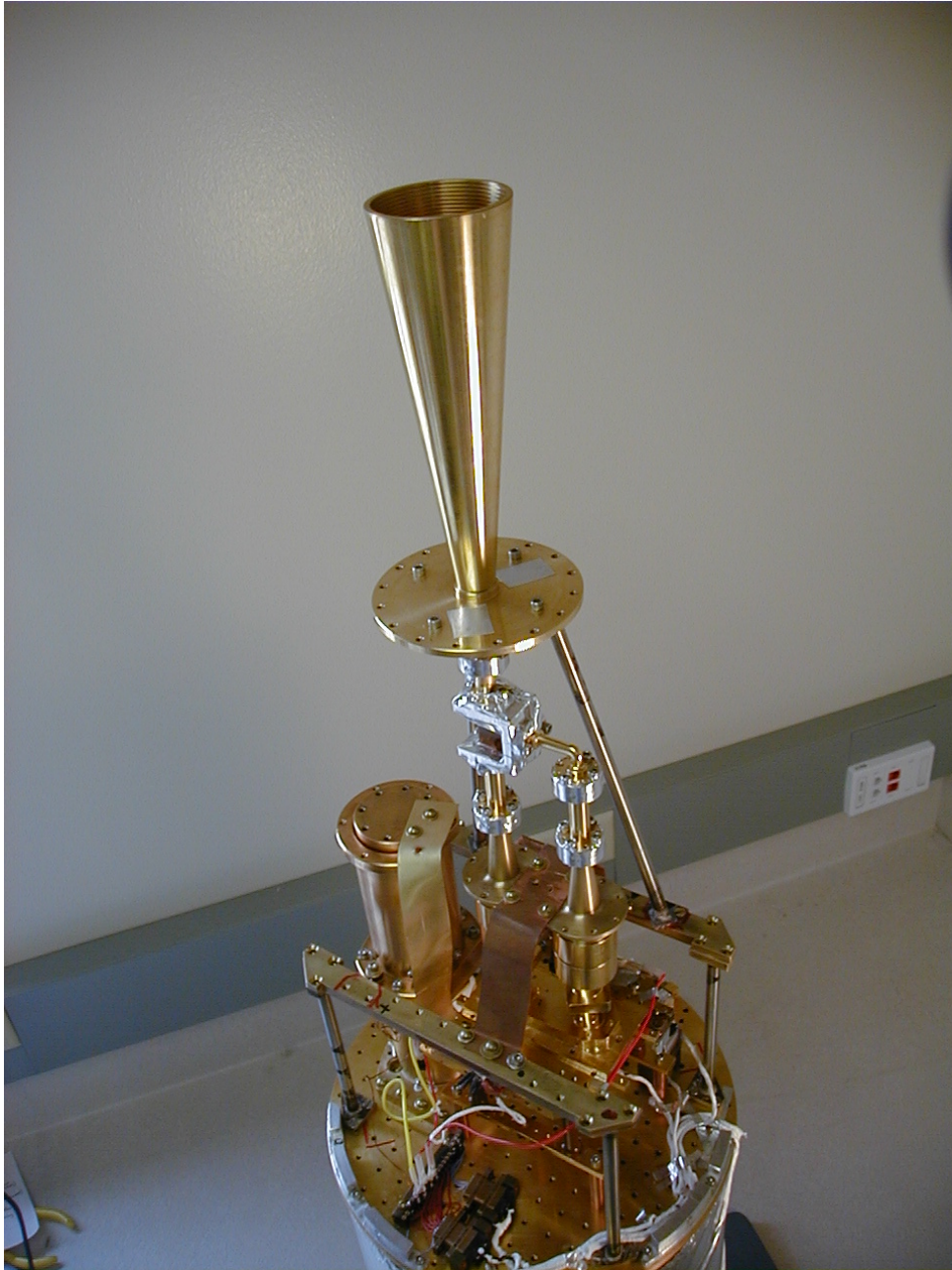[1]Infrared Laboratories, Inc., 1808 East 17th Street, Tucson, AZ 85719-6505

Figure 5.1: A photo of the Polatron focal plane within the HDL-8 test bed.

chopped source, a mylar beam-splitter, and a computer-controlled flat mirror which modulates the interferometric phase difference along its two arms. Two parabolic collimating mirrors increase the signal throughput of the system; the source is placed at the focus of the first mirror, the entrance feed of the instrument under measurement is placed at the focus of the second mirror. The frequency resolution of the FTS is determined by the throw of the positionable flat mirror. For a fixed mirror step, higher-resolution measurements require longer scans of the positionable mirror, and hence better low-frequency stability in the instrument. For the Polatron test-bed, scans longer than 20 minutes were useless due to drifts, and so the spectral resolution was limited to 2 GHz, adequate for our purposes.

The measured bands, plotted in Figure 5.2, are identical within the 2 GHz spectral resolution of the FTS measurement. The center frequency ν_0 of the band when observing a source of intensity I_ν is defined as

$$\nu_0 \equiv \frac{\int d\nu\, \nu\, \eta(\nu)}{\int d\nu\, \eta(\nu)}. \tag{5.1}$$

The measured band centers and widths for both channels are $\nu_0 = 98 \pm 2$ GHz and $\Delta\nu = 17 \pm 2$ GHz full width at half maximum (FWHM).

We searched for spectral leaks at frequencies above our band with brass thick grill filters. Thick grill filters are metal plates with drilled holes that act as waveguide chokes at wavelengths above 1.7 times the hole diameter [76]. High-frequency radiation passes through, though with reduced efficiency due to the effective area of the holes. A chopped 300 K / 77 K blackbody load was placed in front of the receiver and the signal was demodulated at the chop frequency. A thick grill filter with calculated low-frequency cutoff at 156 GHz was used. A measured upper limit of 1.0% was placed on out-of-band power compared to in-band power for each channel.

These measurements can be translated into an upper limit on the out-of-band contribution from dust to the brightness temperature that would be measured by the radiometer. Since the detailed spectrum of any leak would be unknown, a worst-case scenario is assumed. We represent high-latitude dust emission by a Rayleigh-Jeans
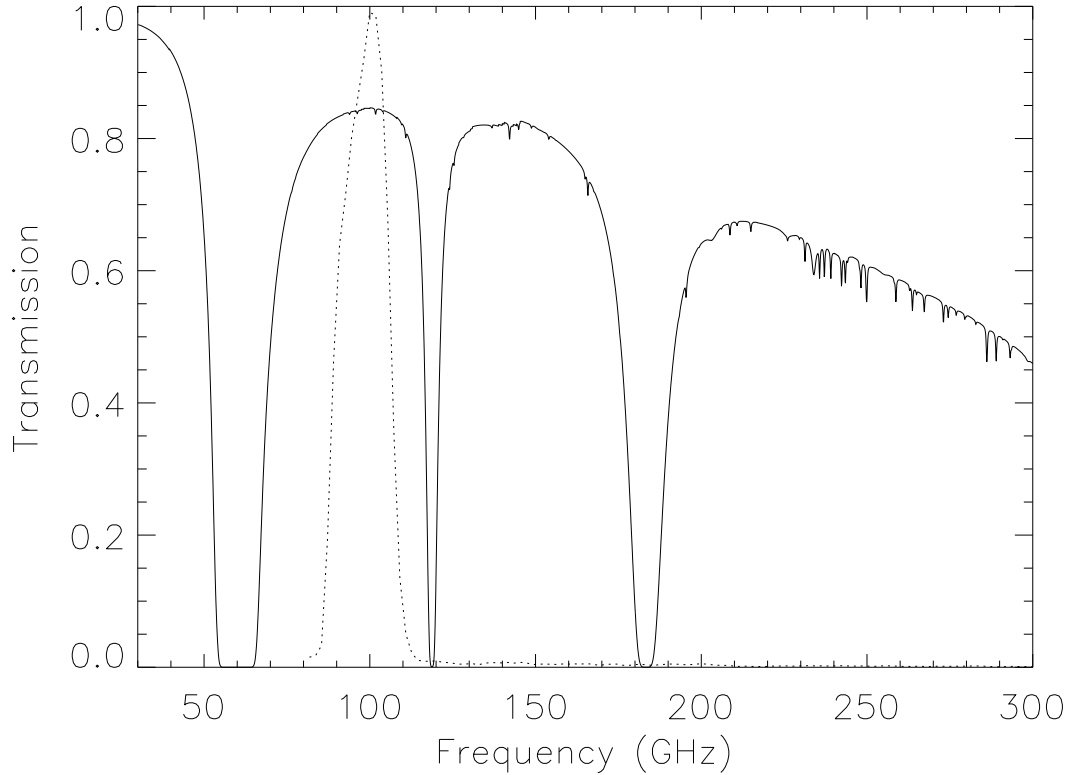
Figure 5.2: Atmospheric Spectrum and Polatron Passband. Solid line: a model atmospheric transmission spectrum for the Owens Valley assuming 6 mm column density of precipitable water vapor. Dotted line: the Polatron passband, in units relative to peak transmission, as measured on a Fourier Transform Spectrometer (FTS). The frequency resolution of the FTS is 2 GHz. The spectral bands for the two orthogonal polarization channels are identical within this resolution.

spectrum with anisotropy temperature 70 μK (following Ruhl [65]) and 10% polarization, an approximation which overestimates the expected power at all frequencies. If the emission from the 77 K and 300 K loads is also assumed to be Rayleigh-Jeans at all frequencies, we can use the thick-grill measurement to set an upper limit of T = 0.07 μK to the anticipated out-of-band contribution from dust.

5.3 Optical Efficiency

The spectral band-averaged optical (photon) efficiency η_{opt} of the receiver is measured by filling the beam with 300 K and 77 K blackbody loads, measuring the power on each detector for each load, and comparing the measured power difference to the expected power difference,

$$\Delta P_{opt} \sim \Delta\nu \frac{\eta_{opt}}{2}(A\Omega)\left[B_{\nu_0}(300K) - B_{\nu_0}(77K)\right]. \tag{5.2}$$

The factor of $1/2$ accounts for the split in polarization, $A\Omega = \lambda^2$ is the throughput of the system, and $B_\nu(T)$ is the Planck blackbody spectrum.

The measured optical power P_{opt} is determined as follows. The system is exposed to beam-filling radiation from $T_{high} = 300$ K and $T_{low} = 77$ K "blackbody" materials, in this case Eccosorb foam[2]. For the 77 K measurement the foam is immersed in liquid nitrogen. In each measurement, the bolometer impedance R_{bolo} is measured as a function of applied electrical bias power $P_{bias} = V_{bolo}^2/R_{bolo}$. The bolometer resistance depends almost entirely on bolometer temperature, and hence on total applied power $P_{opt} + P_{bias}$[3]. At equal bolometer resistance, the total applied power is the same, and so the difference in optical power ΔP_{opt} is the measured difference in electrical power ΔP_{bias}. The measurement is repeated for a range of applied powers.

In this way, we measure band-averaged optical efficiencies of $20.0\% \pm 2.5\%$ for both channels. We assume that nearly all of the loss in our feed structure takes place in the cold filtering and at the detector itself. The wave plate is anti-reflection coated to minimize loss, achieving a measured insertion loss of $< 1\%$. The feed horn, OMT, and associated waveguide components were separately measured warm on a high-frequency network analyzer and found to generate $< 1\%$ return loss across the spectral band.

---

[2]EV Roberts, 8500 Stellar Drive, P.O. Box 868, Culver City, CA 92032

[3]There is an additional, smaller dependence of resistance on bias voltage (the "electric field effect") which must be accounted for [63].

5.4 Polarization Efficiency

To measure the polarization efficiency, we constructed a polarized source by placing a 10 cm diameter circular aperture grid of 0.05 mm diameter gold-plated tungsten wire with 0.19 mm grid spacing in front of a chopped 300 K / 77 K blackbody load. A piece of absorbing material was placed in front of the grid to limit the aperture to ~ 5 cm circular diameter. The source was placed on the optic axis, approximately 10 cm from the entrance of the receiver. Locking-in to the chopped signal, the wave plate was rotated in 128 steps through $360°$ (see Figure 5.3). Since $> 99.5\%$ polarization is produced by the wire grid [47], the degree to which the lock-in signal does not fall to zero is the measured cross-polarization $\chi = 1 - \eta_{pol}$. In this way we measure a laboratory polarization efficiency of $\eta_{pol} = 97.8\% \pm 0.7\%$, in good agreement with an heuristic calculation (see Appendix A).

The polarization efficiency of the receiver optics was measured in a similar manner, with the wave plate removed and the wire grid source rotated through $360°$. The measured polarization efficiency was $\eta_{pol} = 99.5\% \pm 0.7\%$, confirming that the dominant source of cross-polarization in our receiver is the passage of signal through the wave plate. The OMT and associated waveguide components were separately measured warm on a high-frequency network analyzer and found to generate $< 0.03\%$ cross-polarization across the spectral band.

Bolometer responsivity depends on the level of optical loading. For a large wire-grid source, rotation of the grid through $360°$ could modulate the amount of power on the bolometer, since the bolometers can detect their 4 K optics in reflection. This would under-estimate the polarization efficiency since the bolometers would be more responsive during the measurement of highest cross-polarization. By limiting the size of the source and measuring the DC-level of the bolometers (in order to track the responsivity), we could be sure that the bolometer responsivity remained the same throughout the measurement.
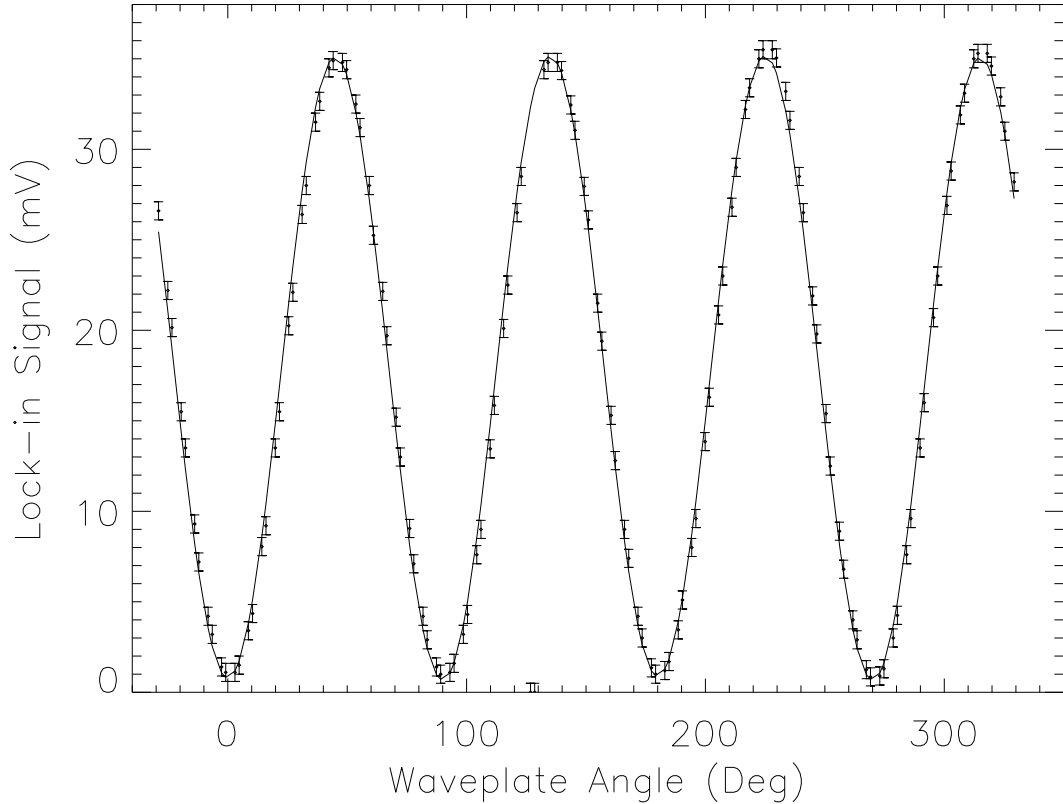
Figure 5.3: Polarization Efficiency Measurement. Depicted is the result of the polarization efficiency measurement described in the text. Error bars are 2-σ. Best fit function is $0.8 + 34.4\sin(4f) - 0.2\sin(2f - 5.6°) + 0.1\sin(f)$ mV; the measured polarization efficiency is $(97.8 \pm 0.7)\%$.

5.5 Detector Properties

The Polatron bolometers possess thermal and electrical properties chosen to provide high sensitivity under the optical loading conditions and operating temperatures specific to the experiment. They were previously flown as science detectors aboard the BOOMERANG payload in 1998. The detectors have a measured response time $\tau = 25$ ms, which puts an upper limit on the allowable frequency of modulation of the signal at $f \sim (2\pi\tau)^{-1} \sim 6$ Hz. The measured thermal conductivities G are ~ 80 pW/K at 0.4 K, and the peak electrical responsivities S are $\sim 3 \times 10^8$ V/W [13] under loading conditions similar to those expected at the telescope.

5.6 Sensitivity

Although the HDL-8 dewar and readout electronics were not designed to be used for actual observations, we measured a raw detector sensitivity for this system as a baseline for future improvements. Bolometer noise spectra were measured looking into a 77 K blackbody load, which is a fair approximation to the ~ 60 K loading temperature expected at the telescope. The low-frequency signal is dominated by 1/f noise with a knee at ~ 1 Hz. This noise arises in the JFET source-follower, as the detectors are not placed in an AC-bridge. The measured bolometer NEP at $f_{wp} = 0.6$ Hz is $\sim 30 \times 10^{-17}$ W Hz$^{-1/2}$. As calculated in §2.5, and under similar observing conditions, this would amount to an NET$_{cmb} \sim 3.2$ mK s$^{1/2}$. If we were observing with this test receiver, we would choose a higher wave plate rotation frequency, out of the 1/f noise but beneath the low-pass cutoff due to the bolometer response time. Such a minimum in the noise spectrum exists at 4 Hz. There we measure a bolometer NEP of $\sim 10 \times 10^{-17}$ W Hz$^{-1/2}$, which would amount to an NET$_{cmb} \sim 1$ mK s$^{1/2}$, comparable to the idealized polarimeter of §4.1.

Chapter 6 Laboratory Characterization — Cryogenics

Substantial cryo-engineering effort has been invested in this instrument to recent and successful end. The cryogenic system went through several incarnations; this chapter and thesis describe the current incarnation and the results achieved for that system alone. We describe here the performance of the cryocooler and multistage sorption coolers.

6.1 Introduction

We have integrated a commercial 4 K mechanical cryocooler with a custom sub-Kelvin multistage sorption cooler to achieve turnkey cooling from 300 K to 0.25 K. Performance measurements of the system were hampered by numerous factors:

- *Turn-around time.* The time between independent measurements depends on the warm-up and cool-down time of the instrument. These in turn depend on the heat capacity of, and thermal conductivity to, various suspended temperature stages, as well as the cooling power available at each stage. Total turn-around time for the Polatron is about one week.

- *Measurement error.* Load curves are generated by applying power to a heater resistor attached to a temperature stage, then measuring the temperature (usually with diode or resistance thermometers) at affected stages. Heaters and thermometers, as well as their lead wires, must be properly heatsunk. Heatsinking becomes increasingly difficult at low temperatures due to the increase in thermal boundary (Kapitza) resistance.

- *Cryogenic and vacuum leaks.* Small leaks in the mechanical cryocooler or multistage sorption cooler will not only eventually exhaust their helium supplies,
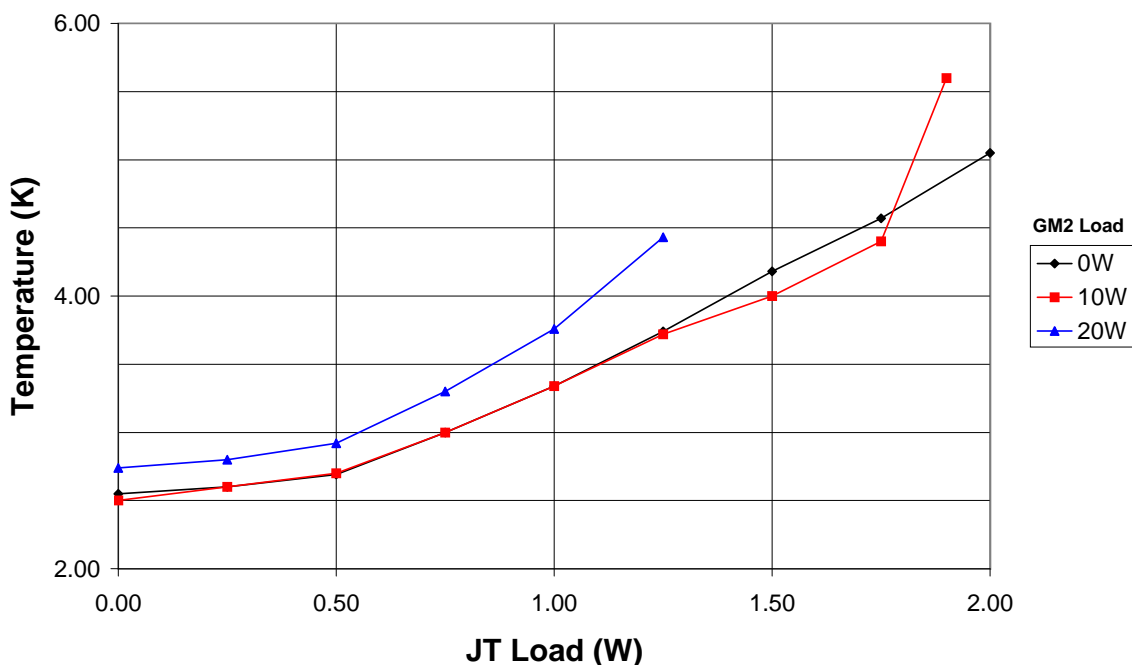
Figure 6.1: Measured load lines on the JT stage of the mechanical cryocooler. The JT aperture was throttled for peak performance at every load point. Lines for varying heat loads on the 50 K 1$^{\text{st}}$ GM stage are shown.

but will also introduce thermally conducting particles into the vacuum space.

6.2   Mechanical Cryocooler

The APD HS-4 mechanical cryocooler advertised 1 W cooling performance at 4 K. As anticipated, cooling performance depends on the (controllable) aperture size of the JT nozzle. Under conditions of higher load, greater cooling can be achieved through a larger JT aperture. The cooling power also depends on the temperature of the precooling GM stages, which in turn depend on their applied heat load. Measured JT stage load lines for a series of GM-stage heat loads are plotted in Figure 6.1.

In the three years of regular use of this cryocooler, we warmed up the system three times due to what we believed to be a clog in the JT nozzle caused by impurities in

the JT helium system. In each of these instances, the symptom was an inability of the system to achieve 4 K temperatures despite standard throttling of the JT aperture on cooldown. In each instance, subsequent cooldowns were without incident.

6.3   Multistage Sorption Cooler

The multistage sorption cooler was successfully operated off of the 4 K base temperature provided by the mechanical cryocooler. The UC still attained a base temperature of 0.24 K and a temperature of 0.25 K at the anticipated 0.5 μW load. The duty cycle of the cooler is 93%, with a total hold time of the refrigerator beneath 0.26 K of 37 hours. Load lines on the UC still are shown in Figure 6.2. Figure 6.3 is a time-history of a typical cycling procedure for the cooler.
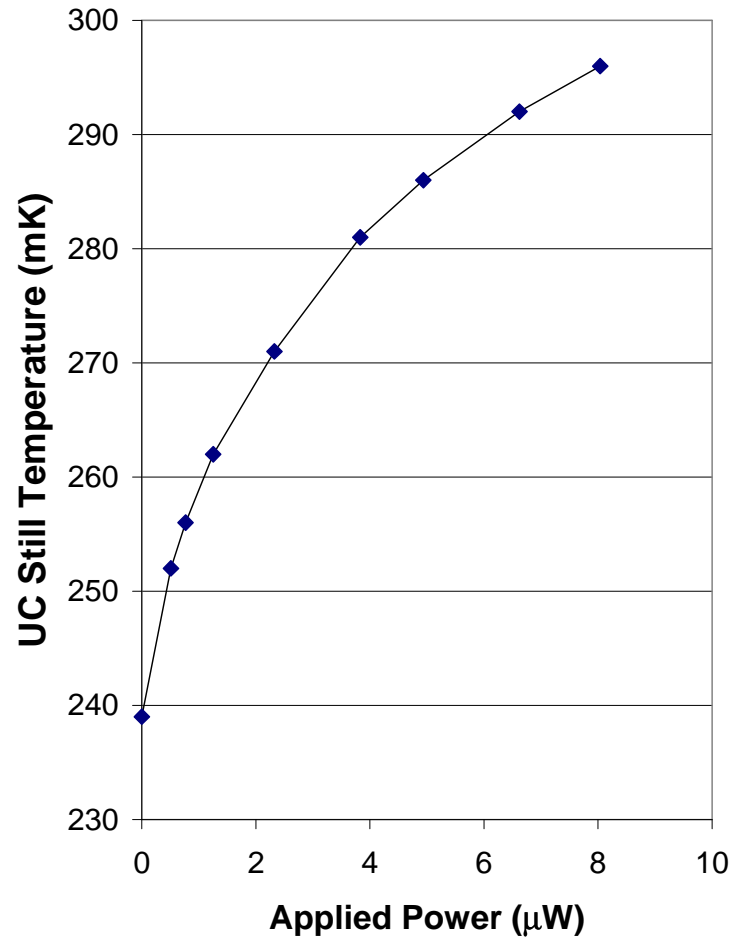
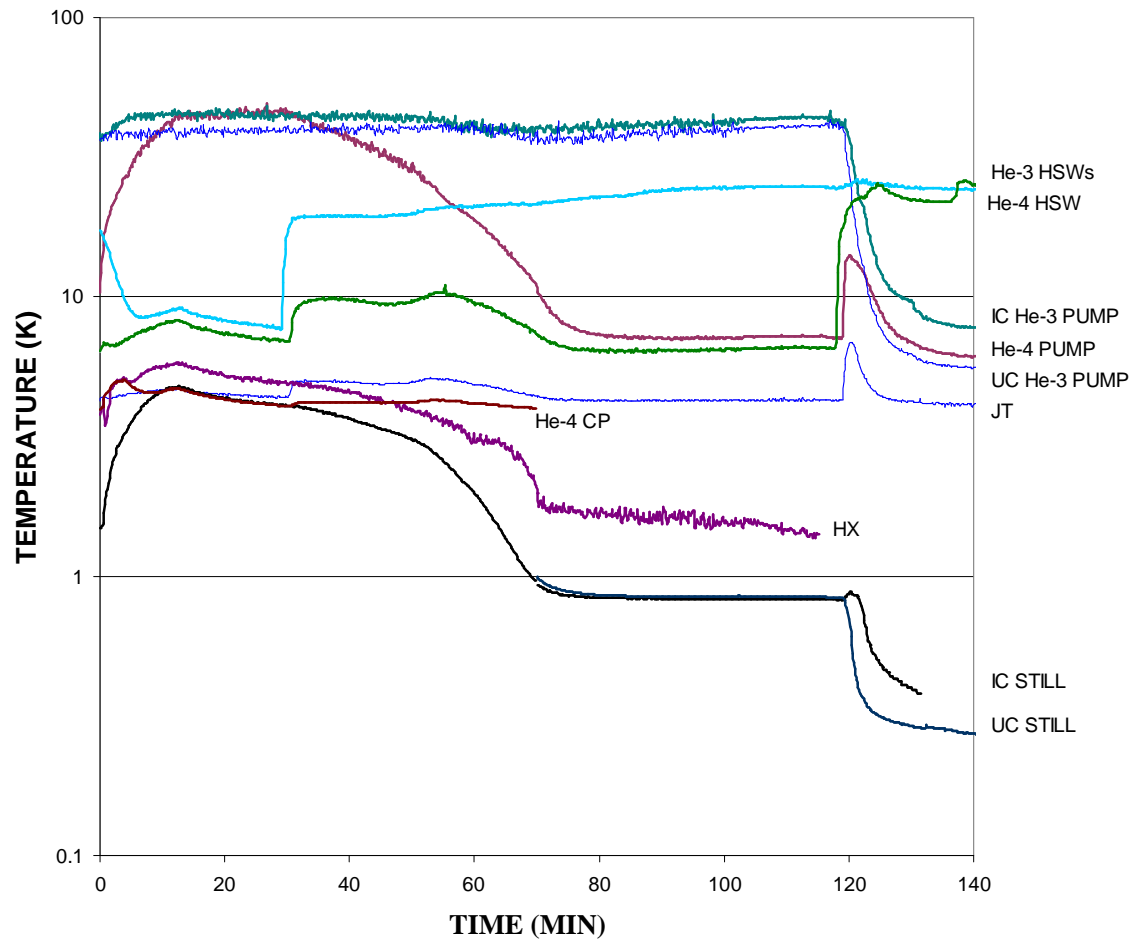Figure 6.2: Load line on UC still of multistage sorption cooler.

Figure 6.3: Time-history of a complete multistage sorption cooler cycling procedure. A base temperature of 0.25 K is obtained after 140 minutes.

Chapter 7   Further Work and Discussion

This thesis has aimed to motivate the variety of experimental efforts being made to detect and characterize the polarization of the cosmic microwave background, and demonstrate the abilities of the Polatron experiment to carry out one such effort. Although improvements in detector technology have revolutionized the field of CMB research, measurement of CMB polarization will require substantial integration time. The Polatron has combined an ambitious scientific goal with a difficult engineering task: fabrication of a cryogenic system which allows autonomous observation of CMB polarization over very long periods of time.

The most significant results presented in this thesis are as follows:

- We have designed and built a bolometric millimeter-wavelength polarimeter with demonstrated ~ 1 mK $\sqrt{s}$ sensitivity, high ($> 95\%$) polarization efficiency, and a powerful polarization modulation technique which employs a half-wave plate to reject systematic polarization effects.

- We have integrated a mechanical cryocooler with a multistage helium sorption refrigerator to provide autonomous, closed-cycle cooling from 300 K to 0.25 K, with adequate cooling power at all stages.

- We have prepared the OVRO 5.5 m telescope for observations at mm-wavelengths by measuring and adjusting the surface accuracy through the use of a capacitive sensor array.

- We have designed an observing scheme which aims to achieve maximum polarization signal by matching the l-space window function of the experiment to the predicted peaks of the polarization power spectrum.

- We have made a careful calculation of the predicted sources of noise for a ground-based bolometric polarimeter, demonstrating that background photon-noise

limited performance can, in principle, be achieved. This calculation strengthens the case for new ground-based polarimeters which rely on common-mode rejection of atmospheric fluctuations.

- We have (in the Appendix) made heuristic calculations of half-wave plate cross-polarization due to chromaticity and off-angle response. These calculations lay a groundwork for more detailed calculations which may be required for the design and fabrication of achromatic plates for multifrequency experiments.

The following work remains before the Polatron can be fielded:

- Characterization of the noise performance of the bolometers under the vibration conditions caused by the mechanical cryocooler. Preliminary work suggests that the vibration-induced detector noise is too high for the observing strategy we propose. An investigation is underway to experimentally determine and mitigate the vibration path from the cryocooler cold tip to the bolometer stage.

- Characterization of the performance of cold optical components under vibration. Measurements are being made at a variety of tilt angles to investigate the influence of the gravity vector on the stiffness of all structures. Varying optical misalignment due to vibration will be analyzed and mitigated.

In the long-term, the Polatron provides a cryogenic and data-acquisition platform for which the focal plane can be modified once the initial science goals of the experiment are met. For instance, if the receiver were placed in an upward-looking position at a dry location, it could carry out an investigation of polarization at large angular scales with little human intervention.

Ultimately, multi-frequency observations of CMB polarization will be required to rule out contamination of signal by galactic foregrounds. The receiver itself can be modified to observe in many frequency bands, utilizing an achromatic half-wave plate to retain the strong rejection of systematic effects such plates allow. It is unlikely that the 5.5 m telescope would be useful at higher frequencies due to the surface inaccuracy.

However, the physical size of the receiver does not preclude its installment at alternate sites.

Appendix A   Half Wave Plates

In this Appendix we review the optical properties of half-wave plates and calculate the expected polarization efficiency of our plate.

The half-wave plate is a cylinder of birefringent, x-cut crystalline quartz. The plate generates a π phase retardation between electric field vectors of frequency $\nu_0 \sim$ 96 GHz (wavelength $\lambda \sim 3$ mm) incident on the fast and slow refraction axes of the quartz. The measured difference in index of refraction along the two axes at these wavelengths is $\Delta n = 0.048$, where $n \sim 2.08$. The differential phase shift $\Delta\phi$ generated between orthogonally polarized rays aligned with the fast and slow axes of the plate is

$$\Delta\phi = \frac{2\pi\nu}{c}\Delta n \times l, \tag{A.1}$$

where l refers to the physical path length the rays travel through the plate. For plane waves on the optic axis, l is the thickness of the plate $t = 32.6$ mm, and a phase retardation of π is achieved for $\nu = \nu_0$, the center of our band.

Consider a linearly polarized plane wave travelling in the $\hat{z}$ direction in a coordinate system $(\hat{\mathbf{x}}, \hat{\mathbf{y}})$ fixed to our polarimeter with electric field

$$\overrightarrow{E}(x, y, z, t) = [E_{0x}\hat{\mathbf{x}} + E_{0y}\hat{\mathbf{y}}]\sin(\phi_{z,t}), \tag{A.2}$$

where $\phi_{z,t} = 2\pi(\frac{z}{\lambda} - \nu t)$ is the kinematic component of the phase.

The intensity of such a beam is $I = E_{0x}^2 + E_{0y}^2$, and the Stokes parameters measured by an ideal polarimeter aligned with this coordinate system are $Q_0 = E_{0x}^2 - E_{0y}^2$ and $U_0 = 2E_{0x}E_{0y}$.

The wave is incident on a half-wave plate with polarization angle $\theta = \tan^{-1}(E_{0y}/E_{0x})$ with respect to the fast axis. θ is restricted to the range $[0, \pi]$. A second coordinate system, $(\hat{\mathbf{i}}, \hat{\mathbf{j}})$, is fixed to the plate's fast and slow axes, respectively. In the plate

coordinates, the electric field vector of the incoming wave is

$$\vec{E}(i,j,z,t) = \left\{[E_{0x}\cos(\theta) + E_{0y}\sin(\theta)]\hat{\mathbf{i}} + [E_{0y}\cos(\theta) - E_{0x}\sin(\theta)]\hat{\mathbf{j}}\right\}\sin(\phi_{z,t}).$$
(A.3)

Upon passage through the plate, the phase of the $\hat{\mathbf{j}}$ component is delayed by $\Delta\phi = \frac{2\pi\nu}{c}\Delta n \times t$ with respect to the $\hat{\mathbf{i}}$ component. For $\nu = \nu_0$, $\Delta\phi = \pi$ and so the $\hat{\mathbf{j}}$ term simply flips sign. In other words, the polarization vector has been reflected about the fast axis, which is equivalent to a rotation by $\Delta\theta = -2\theta$. Converting back to the polarimeter coordinate system,

$$\vec{E'}(x,y,z,t) = \left\{[E_{0x}\cos(2\theta) + E_{0y}\sin(2\theta)]\hat{\mathbf{x}} + [E_{0y}\cos(2\theta) - E_{0x}\sin(2\theta)]\hat{\mathbf{y}}\right\}\sin(\phi_{z,t}).$$
(A.4)

The Stokes parameters are rotated by 4θ:

$$
\begin{aligned}
Q' &= [E_{0x}\cos(2\theta) + E_{0y}\sin(2\theta)]^2 - [E_{0y}\cos(2\theta) - E_{0x}\sin(2\theta)]^2 &\text{(A.5)} \\
&= Q_0\cos(4\theta) + U_0\sin(4\theta), &\text{(A.6)}
\end{aligned}
$$

and

$$U' = U_0\cos(4\theta) - Q_0\sin(4\theta).$$
(A.7)

A.1 Wave Plate Cross-polarization for $\nu \neq \nu_0$

Consider a polarized beam of intensity I_0 incident on the wave plate with polarization vector $\hat{\mathbf{y}}$ aligned at a 45° angle to the fast ($\hat{\mathbf{i}}$) and slow ($\hat{\mathbf{j}}$) axes of the plate. For frequency ν_0 the polarization will be rotated by 90°, into the $\hat{\mathbf{x}}$ direction, and a polarization detector aligned with $\hat{\mathbf{y}}$ will measure no signal. For frequencies $\nu \neq \nu_0$ the wave plate is less efficient, and some cross-polar signal will be detected. The electric field incident on the plate is

$$\vec{E}(i,j,z,t) = \frac{E_0}{\sqrt{2}}\sin(\phi_{z,t})\left[\hat{\mathbf{i}} + \hat{\mathbf{j}}\right].$$
(A.8)

The phase retardation for the polarization component aligned with the slow axis is $\Delta\phi = \frac{2\pi\nu}{c}\Delta n \times t = \pi + \delta\phi$, where $\delta\phi = \pi((\nu/\nu_0) - 1)$. Upon passage through the plate,

$$\overrightarrow{E}(i,j,z,t) = \frac{E_0}{\sqrt{2}}\left[\sin(\phi_{z,t})\hat{\mathbf{i}} + \sin(\phi_{z,t} + \pi + \delta\phi)\hat{\mathbf{j}}\right], \tag{A.9}$$

$$= \frac{E_0}{\sqrt{2}}\left[\sin(\phi_{z,t})\hat{\mathbf{i}} - \sin(\phi_{z,t} + \delta\phi)\hat{\mathbf{j}}\right]. \tag{A.10}$$

The projection of this vector along the detector ($\hat{\mathbf{y}}$) direction is

$$\overrightarrow{E} \cdot \hat{\mathbf{y}} = \frac{E_0}{2}\left[\sin(\phi_{z,t}) - \sin(\phi_{z,t} + \delta\phi)\right] \tag{A.11}$$

$$= \frac{E_0}{2}\left[\sin(\phi_{z,t}) - \sin(\phi_{z,t})\cos(\delta\phi) - \cos(\phi_{z,t})\sin(\delta\phi)\right]. \tag{A.12}$$

The detector is sensitive to the time average of the square of the electric field,

$$\langle|\overrightarrow{E} \cdot \hat{\mathbf{y}}|^2\rangle = I_0 \times \frac{1}{2}\left[1 - \cos(\delta\phi)\right]. \tag{A.13}$$

The total fractional cross-polarization seen by a detector with spectral response $\eta(\nu)$ aligned along the $\hat{\mathbf{y}}$ direction is then

$$\chi = \frac{\int_0^\infty d\nu\,\eta(\nu)I_0(\nu) \times \frac{1}{2}[1 - \cos(\delta\phi)]}{\int_0^\infty d\nu\,\eta(\nu)I_0(\nu)}. \tag{A.14}$$

With the measured spectral response of the Polatron receiver, Eqn. #A.14 predicts a cross-polarization $\chi = 0.9\% \pm 0.1\%$ ($\eta_{pol} = 1 - \chi = 99.1\% \pm 0.1\%$), where the error is dominated by the accuracy of the measurement of the spectral band near the band edges. The same calculation with a model Gaussian spectral band with band center and width equal to the measured Polatron values predicts $\chi = 0.8\%$ ($\eta_{pol} = 99.2\%$).

A.2 Wave Plate Cross-polarization Due to Converging Beam

Placement of the wave plate in a converging beam generates cross-polarization since different parts of the beam travel through different thicknesses of quartz, and experience different phase shifts. Modelling this effect can be quite involved, since the wave plate is in the near field of a single-mode gaussian beam with a changing phase profile. Since the expected cross-polarization is fairly low, a simple calculation can help us to understand the basic performance.

Consider a polarized beam of intensity I_0 incident on the wave plate at angle θ with respect to normal, and with polarization vector $\hat{\mathbf{y}}$ aligned at a 45° angle to the fast ($\hat{\mathbf{i}}$) and slow ($\hat{\mathbf{j}}$) axes of the plate. The phase shift upon passage through the plate is $\Delta\phi = \frac{2\pi\nu}{c}\Delta n \times t \sec(\theta) = \pi + \delta\phi$, where $\delta\phi = \pi(\sec(\theta) - 1)$. The response of a polarization detector aligned with $\hat{\mathbf{y}}$ is as shown in equation (A13).

The angular response $g(\theta)$ of the feed horn at a distance z from the horn phase center (focus) can be estimated as in Wylde et al. [78]:

$$g(\theta) \propto e^{-\theta^2 (z/w(z))^2}, \tag{A.15}$$

where

$$w(z) = w_0 \times \left[1 + \left(\frac{\lambda z}{\pi w_0^2}\right)^2\right]^{1/2}, \tag{A.16}$$

$w_0 = 0.64\,a$, and a is the aperture radius of the feed horn.

The total fractional cross-polarization seen by the detector is then

$$\chi = \frac{\int_0^{\frac{\pi}{2}} d\theta\, 2\pi\theta\, g(\theta) \times \frac{1}{2}[1 - \cos(\delta\phi)]}{\int_0^{\frac{\pi}{2}} d\theta\, 2\pi\theta\, g(\theta)}. \tag{A.17}$$

This predicts $\chi \sim 0.5\%$ ($\eta_{pol} = 99.5\%$) for the Polatron receiver. In combination with the calculation of cross-polarization due to the Polatron spectral bandwidth, a total polarization efficiency for the receiver of $\eta_{pol} \sim 98.5\%$ is predicted. The

measured efficiency is $97.8\% \pm 0.7\%$ (§5.4).

Bibliography

[1] Ade, P.A.R. 2001, personal communication

[2] Barren, R.F. 1985, Cryogenic Systems (Oxford University Press: New York)

[3] Bhatia, R.S., et al., in Proc. of the 11th International Cryocooler Conf., ed. R.G. Ross, Jr. (New York: Plenum Press), 577

[4] Bhatia, R.S. 1998, Ph.D. Thesis (Queen Mary and Westfield College, London)

[5] Bhatia, R.S., et al. 1999, Cryogenics, 39, 701

[6] Bouchet, F.R., et al. 1999, New Astronomy, 4, 443

[7] Cartwright, J.K. 2001, personal communication

[8] Chandrasekar S. 1960, Radiative Transfer (New York: Dover)

[9] Chattopadhyay, G., et al., 1998, IEEE Microwave and Guided Wave Letters

[10] Church, S.E. 1995, MNRAS, 272, 551

[11] Church, S.E., Philhour, B.J., Lange, A.E., Ade, P.A.R., Maffei, B., Nartallo-Garcia, R., & Dragovan, M. 1996, in Conf. Proc. 30th ESLAB Symposium (Noordwijk: ESTEC)

[12] CMBFAST, see: *http://www.physics.nyu.edu/matiasz/CMBFAST/cmbfast.html*

[13] Crill, B.P. 2000, Ph.D. Thesis (California Institute of Technology)

[14] Crittenden, R.G., Coulson, D., & Turok, N.G. 1995, Phys Rev D, 52, 5402

[15] Danese, L., & Partridge, R.B. 1989, ApJ, 342, 604

[16] de Bernardis, P., et al. 1999, New Astronomy Reviews, 43, 289

[17] Delabrouille, J., Gorski, K.M., & Hivon, E. 1998, MNRAS, 298, 445

[18] Dragone, C. 1977, Bell System Technical Journal, 56, 835

[19] Draine, B., & Lazarian, A. 1998, ApJ, 494, L19

[20] Duband, L., et al., 1994, Cryogenics 34, 635, and references therein

[21] Glenn, J. 1997, Ph.D. Thesis (University of Arizona)

[22] Halverson, N.W., et al. 2001, ApJ, in press (astro-ph/0104489)

[23] Hecht, E., & Zajac, A. 1982, Optics (Reading: Addison-Wesley)

[24] Hedman, M. M., Barkats, D., Gundersen, J. O., Staggs, S. T., & Winstein, B. 2001, ApJ, 548, L111

[25] Herbig, T., Lawrence, C. R., Readhead, A. C. S., & Gulkis, S. 1995, ApJ Letters, 449, L5

[26] Hildebrand, R., & Dragovan, M. 1995, ApJ, 450, 663

[27] Hobson, M.P. & Magueijo, J. 1996, MNRAS, 283, 1133

[28] Holzapfel, W. L. 1997, Ph.D. Thesis (University of California at Berkeley)

[29] Holzapfel, W. L., Wilbanks, T. M., Ade, P. A. R., Church, S. E., Fischer, M. L., Mauskopf, P. D., Osgood, D. E., & Lange, A. E. 1997, ApJ, 479, 17

[30] Hu, W., & White, M. 1997, New Astronomy, 2, 323

[31] Hu, W. 2001, in preparation (astro-ph/0108090)

[32] Hubble, E. 1929, Proc. N.A.S., 15, 168

[33] Jaffe, A. H., Kamionkowski, M., & Wang, L. 2000, Phys Rev D, 61, 11462d

[34] Jones, W.C 2001, personal communication

[35] Kamionkowski, M., Kosowsky, A., & Stebbins, A. 1997, Phys Rev D, 55, 7368

[36] Kamionkowski, M., Kosowsky, A., & Stebbins, A. 1997, Phys Rev D Letters, 78, 2058

[37] Keating, B., O'Dell, C. W., de Oliveira-Cost, A., Klawikowski, S., Stebor, N., Piccirillo, L., Tegmark, M., & Timbie, P. T. 2001, ApJ, submitted (astro-ph/0107013)

[38] Keating, B., Timbie, P., Polnarev, A., & Steinberger, J. 1998, ApJ, 495, 580

[39] Knox, L. 1995, Phys Rev D, 52, 4307

[40] Kosowsky, A. 1996, Ann. Phys., 246, 49

[41] Lange, A.E., et al. 2001, Phys Rev D, in press (astro-ph/0005004)

[42] Lawrence, C.L., Herbig, T., & Readhead, A.C.S. 1994, Proc. IEEE, 82, 763

[43] Lee, C., Ade, P.A.R., & Haynes, C.V. 1996, in Conf. Proc. 30th ESLAB Symposium (Noordwijk: ESTEC)

[44] Leitch, E. M., Readhead, A. C. S., Pearson, T. J., Myers, S. T., Gulkis, S., & Lawrence, C. R. 2000, ApJ, 532, 37

[45] Leitch, E. M., et al. 2001, ApJ, in press (astro-ph/0104488)

[46] Leong, J. 2001, Undergraduate Thesis (California Institute of Technology)

[47] Lesurf, J.C.G. 1990, Millimetre-wave Optics, Devices and Systems (Bristol: Adam Hilger)

[48] Mason, B. S., Myers, S. T., & Readhead, A. C. S. 2001, ApJ, in press (astro-ph/0101169)

[49] Murray, A.G., et al. 1992, Infrared Physics, 33, 113

[50] Myers, S. T., Readhead, A. C. S., & Lawrence, C. R. 1993, ApJ, 405

[51] Myers, S. T., Baker, J. E., Readhead, A. C. S., Leitch, E. M., & Herbig, T. 1997, ApJ, 485, 1

[52] Netterfield, C. B., Jarosik, N., Page, L., Wilkinson, D., & Wollack, E. 1995, ApJ Letters, 445, L69

[53] Partridge, R. B., Nowakowski, J., & Martin, H. M. 1988, Nature, 331, 146

[54] Olver, A.D. 1992, Electronics & Communication Engineering Journal

[55] Padin, S., Cartwright, J. K., Mason, B. S., Pearson, T. J., Readhead, A. C. S., Shepherd, M. C., Sievers, J., Udomprasert, P. S., Holzapfel, W. L., Myers, S. T., Carlstrom, J. E., Leitch, E. M., Joy, M., Bronfman, L., & May, J. 2001, ApJ Letters, 549, L1-L5

[56] Padman, R., Murphy, J. A., & Hills, R. E. 1987, IEEE Transactions on Antennas and Propagation, AP-35, 1093

[57] Penzias, A. A., & Wilson, R. W. 1965, ApJ, 142, 419

[58] Philhour, B. J., et al., 2001, in preparation (astro-ph/0106543)

[59] Plambeck, R. I. 1995, Proceedings of the 8th Internatinoal Cryocooler Conference, 795

[60] Polnarev, A.G. 1985, Sov. Astron., 29, 607

[61] Prunet, S., Sethi, S. K., & Bouchet, F. R. 2000, MNRAS, 314, 348

[62] Pryke, C., et al. 2001, ApJ, in press (astro-ph/0104490)

[63] Richards, P.L., J. Appl. Phys. 1994, 76, 1

[64] Readhead, A. C. S., Lawrence, C. R., Myers, S. T., Sargent, W. L. W., Hardebeck, H. E., & Moffet, A. T. 1989, ApJ, 346, 566

[65] Ruhl, J. 1993, Ph.D. Thesis (Princeton University)

[66] Runyan, M.C. 2001, personal communication

[67] Ruze, J. 1966, IEEE Proceedings, 54, 663

[68] Seljak, U. & Zaldarriaga, M. 1997, Phys Rev Letters, 78, 2054

[69] Shuman, M.M. 1999, Undergraduate Thesis (California Institute of Technology)

[70] Smoot, G. F, et al., 1992, ApJ, 396, L1

[71] Sunyaev, R. A., & Zel'dovich, Ya. B. 1972, Comments on Astrophysics and Space Physics, 4, 173

[72] Staggs, S. T. et al. 1999, ASP Conf. Ser. 181: Microwave Foregrounds, 299

[73] Stompor, R., et al. 2001, ApJ, in submission (astro-ph/0105062)

[74] Tegmark, M. 1997, Phys Rev D, 56, 4514

[75] Tegmark, M., & de Oliveira-Costa, A. 2000, in preparation (astro-ph/0012120)

[76] Timusk, T., & Richards, P.L. 1981, Applied Optics, 20, 1355

[77] Wilbanks, T., Devlin, M., Lange, A.E., Sato, S., Beeman, J.W., & Haller, E.E. 1990, IEEE Transactions on Nuclear Science, 37, 566

[78] Wylde, R.J. 1984, IEEE Proceedings, 131, 258

[79] Zaldarriaga, M., & Seljak, U., 1997, Phys Rev D, 55, 1830

[80] Zaldarriaga, M. 1998, ApJ, 503, 1

[81] Zaldarriaga, M. 1998, Ph.D. Thesis (Massachusetts Institute of Technology)